

Model form uncertainty quantification of Reynolds-averaged Navier-Stokes modeling of flows over a SD7003 airfoil

Minghan Chu,^{1, a)} Xiaohua Wu,^{1, b)} and David E. Rival²

¹⁾*Mechanical and Aerospace Engineering, Royal Military College of Canada, Kingston, ON K7K 7B4, Canada.*

²⁾*Mechanical and Materials Engineering Department, Queen's University, Kingston, ON K7L 2V9, Canada.*

(*Electronic mail: 17mc93@queensu.ca.)

(Dated: 1 August 2022)

It is well known that the Boussinesq turbulent viscosity hypothesis can yield inaccurate predictions when complex flow features are involved, e.g. laminar-turbulent transition. The focus of the study is to explore the capability of a physics-based uncertainty quantification (UQ) approach to quantify the model-form uncertainty in Reynolds-averaged Navier-Stokes (RANS) simulations of laminar-turbulent transitional flows over an Selig-Donovan (SD) 7003 airfoil. This methodology perturbs the modeled Reynolds stress tensor in the momentum equations; perturbations are injected into the amplitude, eigenvalues and eigenvectors of the anisotropy Reynolds stress tensor undergone an eigen-decomposition. In this study, our analyses focus upon the amplitude perturbation. We observed a monotonic behavior of the magnitude of the predicted uncertainty bounds for different quantities of interest. High-order regressions based on the turbulence kinetic energy discrepancies are used to develop a novel switch marker function M_k to introduce perturbations in a non-uniform manner over different regions of the domain based upon prior knowledge of the limitations of the model. Importantly, the compound effect of M_k and eigenvalue perturbations show a synergy behavior, e.g., dramatically increased uncertainty bounds to account for the discrepancy in the RANS prediction; and the M_k function effectively avoids over-perturbation to the amplitude of the anisotropy Reynolds stress tensor. In this context, regression based amplitude perturbation of the anisotropy Reynolds stress tensor makes a new contribution to the RANS UQ methodology in the simulations of the airfoil transitional flows, which shows very encouraging results.

I. INTRODUCTION

Transitional flow regime is very frequently encountered in turbomachines and especially in aircraft engines at relatively low Reynolds numbers. As a consequence, a significant part of the flow on the blade surfaces is under the laminar-turbulent transition process. The boundary development, losses, efficiency, and momentum transfer are greatly affected by the laminar-turbulent transition. Therefore, accurate prediction for the transition process is crucial for the design of efficient as well as reliable aerospace designs¹.

RANS simulations remain the most commonly used computational technique for analysis of turbulent flows. There has been considerable effort spent in the past two decades to develop RANS based transition models for engineering applications to predict various kinds of transitional flows²⁻⁸. Each model has its strengths and weaknesses, and by far the correlation-based transition models by Langtry and Menter^{5,6} have been widely used in engineering industries, in particular, aerospace industry. Most RANS models have adopted the Boussinesq turbulent viscosity hypothesis, i.e., anisotropy Reynolds stresses are proportional to the mean rate of strain, therefore also referred to as linear eddy viscosity models. It is well known that linear eddy viscosity models are limited

due to the restrictions of the Boussinesq turbulent viscosity hypothesis on yielding accurate predictions for complex flow features such as flow with significant streamline curvature, separation, reattachment, and laminar-turbulent transition. Large eddy simulations (LES) or Direct numerical simulations (DNS) provide high-fidelity solution for such problems, but the calculations are often too expensive in computational time and cost, especially for high-Reynolds number flows. Therefore, accounting for the errors and uncertainties in the RANS model predictions provides a means to quantify trust in the predictions, as well as enabling the application of robust and reliability based design optimization. More expensive LES or DNS would only be considered necessary if the model form uncertainty is too large.

The current study considers a physics-based approach that has been recently introduced by Emory *et al.*⁹, namely eigenspace perturbation method. This framework quantifies the model form uncertainty associated with the linear eddy viscosity model via sequential perturbations in the predicted amplitude (turbulence kinetic energy), shape (eigenvalues), and orientation (eigenvectors) of the anisotropy Reynolds stress tensor. This is an established method for RANS model UQ and has been applied to analyze and estimate the RANS uncertainty in flow through scramjets¹⁰, aircraft nozzle jets, turbomachinery, over stream-lined bodies¹¹, supersonic axisymmetric submerged jet¹², and canonical cases of turbulent flows over a backward-facing step^{13,14}. This method has been used for robust design of Organic Rankine Cycle (ORC) turbine cascades¹⁵. In aerospace applications, this method has been used for design optimization under uncertainty¹⁶⁻¹⁹. In civil engineering applications, this method is being used

^{a)}Mechanical and Materials Engineering Department, Queen's University, Kingston, ON K7L 2V9, Canada.

^{b)}<https://www.rmc-cmr.ca/en/mechanical-and-aerospace-engineering/xiaohua-wu>

to design urban canopies²⁰, ensuring the ventilation of enclosed spaces, and used in the wind engineering practice for turbulent bluff body flows²¹. This perturbation method for RANS model UQ has been used in conjunction with Machine Learning algorithms to provide precise estimates of RANS model uncertainty in the presence of data^{22–28}. The method is also being used for the creation of probabilistic aerodynamic databases, enabling the certification of virtual aircraft designs^{29,30}.

All of the aforementioned studies that adopted the eigenspace perturbation framework focused on eigenvalue and eigenvector perturbations but did not consider the turbulence kinetic energy perturbation. According to Mishra and Iaccarino³¹, turbulence kinetic energy perturbation varies the coefficient of turbulent viscosity in the Boussinesq turbulent viscosity hypothesis. Currently all eddy viscosity models utilize a predetermined constant value of this coefficient. In reality, the coefficient of turbulent viscosity varies between different turbulent flow scenarios and even between different regions in the same turbulent flow³¹. Therefore, perturbing the amplitude of the anisotropy Reynolds stress tensor not only captures the full ranges of uncertainties introduced by the Boussinesq turbulent viscosity hypothesis, but plays an important role in capturing the true physics of the turbulent flow. However, studies of turbulence kinetic energy perturbation are lacking. The only studies that have been conducted to address the turbulence kinetic energy perturbation are proposed by^{14,32}. Yet to date, the combined effect of the turbulence kinetic energy and eigenvalue perturbation have not been examined for airfoil flows. It should be noted that introducing uniform perturbations in the entire flow field often lead to overly conservative confidence intervals, because decades of experience in RANS modeling show that the models are not always inaccurate. Consequently, it is reasonable for one to only introduce uncertainties in the regions of the flow where the model is deemed plausibly untrustworthy. Gorré *et al.*³³ first proposed the concept of *ad hoc* “marker function” that identifies regions that deviate from parallel shear flow. A recent study of Gorré *et al.*¹¹ employed this marker function and applied it to the simulation for a flow over a periodic wavy wall. Emory *et al.*⁹ also provided a variety of marker functions aimed at spatially varying the magnitude of the eigenvalue perturbation in a computational domain. Nevertheless, marker function development is still very under-explored and more rigorous discussion and validation of new marker is needed.

There are few methods for implementing the effects of the model form uncertainty on a transitional near-wall flow in a RANS formulation. In this case, the local-correlation laminar-turbulent transition model of Langtry and Menter⁵ is used to close the mean transport equations. It has been extensively used to predict a wide variety of transitional flows such as natural transition and laminar-turbulent transition. However, there are few studies concerning the model form uncertainty in transition modeling.

Therefore, the objective of this paper is to advance the understanding of the performance of the eigenspace perturbation approach for quantifying the model form uncertainty in RANS simulations of transitional flows over a SD7003 airfoil

using the transition model of Langtry and Menter⁵. Specifically, the objectives of this study are (1) to develop a new regression based marker function M_k for the perturbation to the amplitude of the anisotropy Reynolds stress tensor based on the turbulence kinetic energy discrepancy between the RANS and in-house DNS³⁴ datasets; (2) to explore the effect of turbulence kinetic perturbation on various quantities of interests (QoIs) through a sets of uniform perturbations; (3) and to have a thorough understanding of the combined effect of the shape and marker-involved amplitude perturbation to the anisotropy Reynolds stress tensor. A novelty of this study lies in the application of the eigenspace perturbation method to transitional flows, as opposed to fully developed turbulent flows as is done in almost prior investigations.

II. METHODOLOGY

A. Governing equations

The flow was assumed to be two-dimensional and incompressible. The RANS formulation of the continuity and momentum equations is as follows:

$$\frac{\partial \langle U_i \rangle}{\partial x_i} = 0, \quad (1)$$

$$\frac{D \langle U_j \rangle}{Dt} = -\frac{1}{\rho} \frac{\partial \langle P \rangle}{\partial x_j} + \nu \frac{\partial^2 \langle U_j \rangle}{\partial x_i \partial x_i} - \frac{\partial \langle u_i u_j \rangle}{\partial x_i} \quad (2)$$

where $\langle \rangle$ represents time-averaging, ρ is the density, $\langle P \rangle$ is the time-averaged pressure, and ν is the kinematic viscosity. The $\langle U_i \rangle$ are the time-averaged velocity components. Reynolds stress terms in Eqs. 1 - 2, i.e., $\langle u_i u_j \rangle$, are unknowns that need to be approximated using a RANS model. In the results presented in this study for a flow over a SD7003 airfoil, the modified version of shear-stress transport (SST) $k - \omega$ ^{35–38} for transitional flow simulations by Langtry and Menter⁵ is considered. The RANS based transition model⁵ is a linear eddy viscosity model based on the Boussinesq turbulent viscosity hypothesis as follows:

$$\langle u_i u_j \rangle = \frac{2}{3} k \delta_{ij} - 2\nu_t \langle S_{ij} \rangle, \quad (3)$$

where k is the turbulence kinetic energy, δ_{ij} is the Kronecker delta, ν_t is the turbulent viscosity, and $\langle S_{ij} \rangle$ is the rate of mean strain tensor. Results obtained from the RANS based transition model bereft of any perturbations are referred to as “baseline” solutions. In Eq. 3, the deviatoric anisotropic part is

$$\begin{aligned} a_{ij} &\equiv \langle u_i u_j \rangle - \frac{2}{3} k \delta_{ij} \\ &= -\nu_t \left(\frac{\partial \langle U_i \rangle}{\partial x_j} + \frac{\partial \langle U_j \rangle}{\partial x_i} \right) \\ &= -2\nu_t \langle S_{ij} \rangle. \end{aligned} \quad (4)$$

The (normalized) anisotropy is defined by

$$b_{ij} = \frac{a_{ij}}{2k} = \frac{\langle u_i u_j \rangle}{2k} - \frac{\delta_{ij}}{3} = -\frac{v_i}{k} \langle S_{ij} \rangle. \quad (5)$$

B. Eigenspace perturbation method

The Reynolds stress tensor $\langle u_i u_j \rangle$ is symmetric positive semi-definite³⁹, thus it can be eigen-decomposed as follows:

$$\langle u_i u_j \rangle = 2k \left(\frac{\delta_{ij}}{3} + v_{in} \hat{b}_{nl} v_{jl} \right), \quad (6)$$

in which $k \equiv u_i u_i / 2$, v represents the matrix of orthonormal eigenvectors, \hat{b} represents the diagonal matrix of eigenvalues (λ_i), which are arranged in a non-increasing order such that $\lambda_1 \geq \lambda_2 \geq \lambda_3$. The amplitude, the shape and the orientation of $\langle u_i u_j \rangle$ are explicitly represented by k , λ_i , and v_{ij} , respectively. Equations 5 and 6 lead to

$$b_{ij} = -\frac{v_i}{k} \langle S_{ij} \rangle = v_{in} \hat{b}_{nl} v_{jl}. \quad (7)$$

Equation 7 indicates that the Boussinesq turbulent viscosity hypothesis requires that the shape and orientation of $\langle u_i u_j \rangle$ to be determined by $(v_i/k) \langle S_{ij} \rangle$. This assumption implies the a_{ij} tensor is aligned with the $\langle S_{ij} \rangle$ tensor, which is not true in most circumstances in practice, in particular, complex flows, e.g., strongly swirling flows, flow with significant streamline curvature, and flow with separation and reattachment, and thus a source of the model form uncertainty.

The eigenspace perturbation method was first proposed in^{40,41}. To quantify errors introduced by the model form uncertainty, perturbation is injected into the eigen-decomposed Reynolds stress defined in Eq. 6. The perturbed Reynolds stresses are defined as

$$\langle u_i u_j \rangle^* = 2k^* \left(\frac{1}{3} \delta_{ij} + v_{in}^* \hat{b}_{nl}^* v_{jl}^* \right), \quad (8)$$

where k^* is the perturbed turbulence kinetic energy, \hat{b}_{kl}^* is the diagonal matrix of perturbed eigenvalues, and v_{ij}^* is the matrix of perturbed eigenvectors. For eigenvalue perturbations, Pecnik and Iaccarino⁴⁰ proposed a perturbation approach, which enforces the realizability constraints on $\langle u_i u_j \rangle$ via the barycentric map⁴², as shown in Fig. 1, because the map contains all realizable states of $\langle u_i u_j \rangle$. Due to the realizability constraint of the semi-definiteness of $\langle u_i u_j \rangle$, there are three extreme states of componentiality of $\langle u_i u_j \rangle$: one component limiting state (1C), which has one non-zero principal fluctuation, i.e., $\hat{b}_{1c} = \text{diag}[2/3, -1/3, -1/3]$; two component limiting state (2C), which has two non-zero principal fluctuations of the same intensity, i.e., $\hat{b}_{2c} = \text{diag}[1/6, 1/6, -1/3]$; and three component (isotropic) limiting state (3C), which has

three non-zero principal fluctuations of the same intensity, i.e., $\hat{b}_{3c} = \text{diag}[0, 0, 0]$. In addition, the \hat{b}_{1c} , \hat{b}_{2c} , and \hat{b}_{3c} limiting states correspond to the three vertices of the barycentric map. Given an arbitrary point \mathbf{x} within the barycentric map, any realizable $\langle u_i u_j \rangle$ can be determined by a convex combination of the three vertices \mathbf{x}_{ic} (limiting states) and λ_i as follows:

$$\mathbf{x} = \mathbf{x}_{1c} (\lambda_1 - \lambda_2) + \mathbf{x}_{2c} (2\lambda_2 - 2\lambda_3) + \mathbf{x}_{3c} (3\lambda_3 + 1). \quad (9)$$

In order to define the perturbed eigenvalues \hat{b}_{ij}^* , first determine the location on the barycentric map for the Reynolds stresses computed by a linear eddy viscosity model and subsequently inject uncertainty by shifting it to a new location on the barycentric map. In Fig. 1, perturbations toward 1c, 2c, and 3c vertices of the barycentric map shift point O to $B_{1c/2c/3c}$, respectively, which can be written as

$$\mathbf{x}_{B(1c/2c/3c)}^* = \mathbf{x}_O + \Delta_B (\mathbf{x}_{1c/2c/3c} - \mathbf{x}_{B(1c/2c/3c)}), \quad (10)$$

where Δ_B is the magnitude of perturbation. Once the new location is determined, a new set of eigenvalues λ_i can be computed from Eq. 9 and b_{ij} can be reconstructed, which eventually yields $\langle u_i u_j \rangle^*$.

As noted earlier in Eq. 7, the unperturbed anisotropy Reynolds stress tensor is modeled as $b_{ij} = -v_i/k \langle S_{ij} \rangle = v_{in} \hat{b}_{nl} v_{jl}$ or, equivalently, $a_{ij} = -2v_i \langle S_{ij} \rangle = 2k v_{in} \hat{b}_{nl} v_{jl}$. Accordingly, the anisotropy Reynolds stress tensor subject to turbulence kinetic energy perturbation becomes

$$a_{ij}^* = -2v_i^* \langle S_{ij} \rangle = 2k^* v_{in} \hat{b}_{nl} v_{jl}. \quad (11)$$

Because perturbing k does not affect the eigenvalues and eigenvectors of the anisotropy Reynolds stress tensor, the change in the turbulent viscosity hypothesis has to be accounted in the turbulent viscosity coefficient³¹. Comparing the unperturbed anisotropy Reynolds stress tensor to Eq. 11, it is easy to obtain³¹

$$\frac{k^*}{k} = \frac{v_T^*}{v_T}, \quad \text{or equivalently,} \quad v_T^* = \frac{v_T k^*}{k}, \quad (12)$$

where $k^* = k + \Delta_k$. From Eq. 12, turbulence kinetic energy perturbation leads to spatial variation of turbulent viscosity coefficient. Specifically, the relation between the turbulent viscosity and the turbulent viscosity coefficient C_μ is given by

$$v_T = C_\mu \frac{k^2}{\varepsilon}, \quad (13)$$

where ε is the dissipation rate.

Thus, the perturbed turbulent viscosity can be expressed as follows:

$$v_T^* = C_\mu^* \frac{k^{*2}}{\varepsilon}, \quad (14)$$

where $C_\mu^* = C_\mu + \Delta C_\mu$. Substituting Eqs. 13 and 14 into Eq. 12, we get³¹

$$\frac{k}{k^*} = \frac{C_\mu^*}{C_\mu}, \quad \text{or equivalently,} \quad \Delta C_\mu = -\frac{\Delta k C_\mu}{k + \Delta k}. \quad (15)$$

In this study, the turbulence kinetic energy discrepancies between the RANS based predictions and the in-house DNS data³⁴ are modeled by high-order regressions. These regressions generate values of k^* that vary spatially in the computational domain:

$$k^* = k + \Delta k = k M_k, \quad M_k \sim f(x, y). \quad (16)$$

In Eq. 16, M_k is a marker function of the x and y coordinate in a computational domain. Additionally, substituting Eq. 15 into Eq. 16 and rearranging, we get:

$$\frac{1}{M_k} = \frac{C_\mu^*}{C_\mu}. \quad (17)$$

Substituting Eq. 17 to Eq. 15, the relation between M_k and ΔC_μ can be expressed as follows:

$$\Delta C_\mu = \frac{C_\mu(1 - M_k)}{M_k}. \quad (18)$$

Therefore, Eq. 18 provides the underlying model structure of turbulence kinetic energy perturbation with a marker function involved.

A detailed description for the modeling of k^* is presented in Section IV A. In addition, eigenvector perturbations rotate the eigenvectors of the anisotropy Reynolds stress tensor with respect to the principal axes of the mean rate of strain. Recall that the eigenvectors of the anisotropy Reynolds stress tensor are forced to align along the principal axes of the mean rate of strain due to the limitations of the Boussinesq turbulent viscosity hypothesis³⁹. This again violates the true physics of turbulent flow. Consequently, eigenvector perturbations extend the Boussinesq turbulent viscosity hypothesis to anisotropy turbulent viscosity hypothesis. Unlike eigenvalue perturbations, which are strictly constrained by realizability. Eigenvector perturbations are more difficult to be physically constrained in a local sense. In this study, eigenvector perturbations are omitted for brevity. Therefore, the present study restricts the contribution to the amplitude and shape perturbation to the anisotropy Reynolds stress tensor.

C. Eigenspace perturbation framework in OpenFOAM

At present the eigenspace perturbation framework is available only in Stanford University's SU2 CFD suite⁴³ and the TRACE solver of DLR¹⁹. In spite of its utility to the design and simulation community, there are no tested and validated implementations of this framework available in popular CFD software. OpenFOAM⁴⁴ is the most widely used

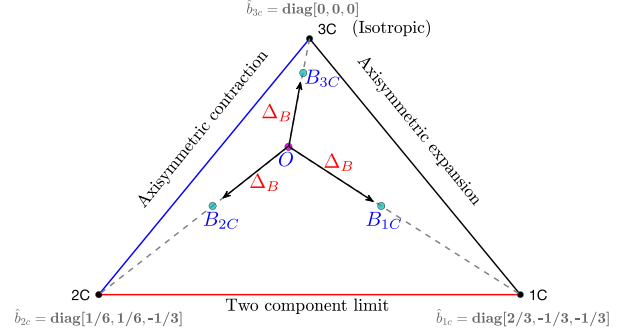


FIG. 1. Barycentric map.

open source CFD software in research and academia. A contribution of this investigation, is the development of a verified and validated implementation of the eigenspace perturbation framework for the OpenFOAM software. Relatively few studies have been conducted to implement the eigenspace perturbation framework in a RANS formulation using OpenFOAM, e.g., see^{14,45}. All of these studies employed the MATLAB software compounded with OpenFOAM to decompose and recompose the Reynolds stress tensor. This increases the complexity of using the eigenspace perturbation framework⁹ in OpenFOAM, which is prone to errors and violating the spirit of versatility. In addition, C++ is inherently faster than Matlab, which reduces the computational expense. In this study, the eigenspace perturbation framework along with the novel marker functions were completely implemented in C++ in OpenFOAM, which greatly reduces the number of user-defined inputs and allows the users without much knowledge of the fluid mechanics to use the eigenspace perturbation framework in OpenFOAM.

In the input files (located under the “constant” directory in OpenFOAM), user needs to specify what magnitude of Δ_B should be assigned, if M_k is needed, and which eigenvalue perturbation (1c, 2c, 3c) is to be performed. The eigenspace framework conducts the perturbations during the execution of simulations, as illustrated in Fig. 2. At each control volume (CV), the baseline Reynolds stress tensor is calculated and decomposed into its eigenvalue and eigenvector matrices, which are perturbed using the eigenspace perturbation method as prescribed earlier. If M_k is involved, perturbation to the turbulence kinetic energy will be performed. The perturbed eigenvalue and eigenvector matrices are then recomposed into a perturbed Reynolds stress tensor for each CV. These perturbed Reynolds stress matrices together with the perturbed turbulence kinetic energy are then used to compute the perturbed velocity field and the perturbed turbulent production to advance each node to the next time step. At convergence, the Reynolds stress also converges to its perturbed state.

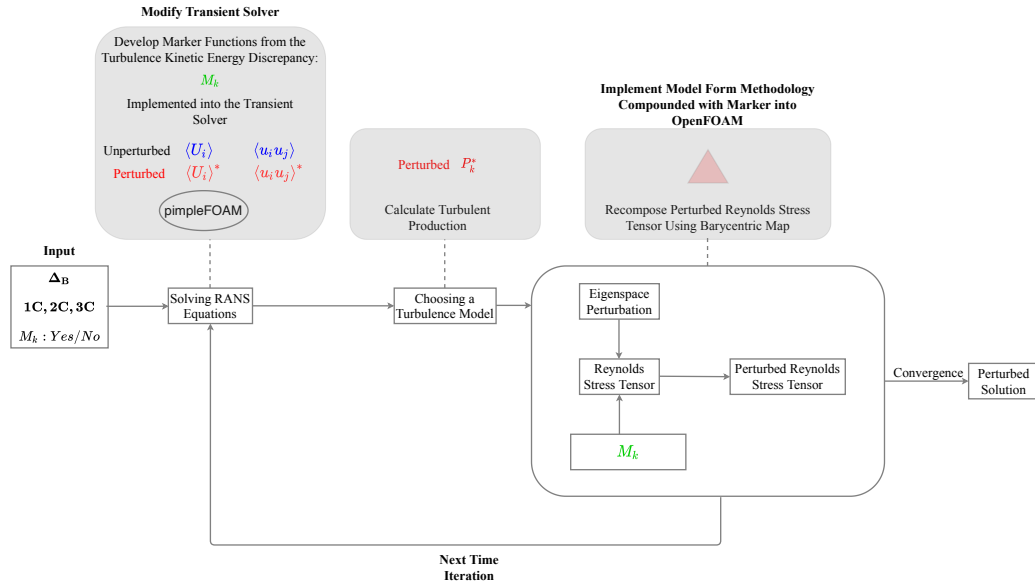


FIG. 2. Flow chart showing the implementation of model form framework within OpenFOAM with marker configuration involved.

III. FLOW DESCRIPTION AND NUMERICAL METHOD

The flow being considered is around an SD7003 airfoil, as shown in Fig. 3. At the low Reynolds number based on the chord length of $Re_c = 60000$, a laminar separation bubble (LSB) is formed on the suction side of the airfoil. Note that the bubble moves upstream as the angle of attack (AoA) increases⁴⁶. In this study, an 8° AoA (nearing stall) was considered. Figure 3 schematically shows that the solution domain is a two-dimensional C-topology grid of 389 (streamwise) \times 280 (wall-normal) \times 1 (spanwise) control volumes, which is comparable to the number of control volumes (768×176) used in the numerical study of⁴⁶. The magnified view of the two-dimensional SD7003 airfoil labels the camber, suction side and pressure side, as shown in Fig. 3. The first grid node to the wall was placed at $y^+ \approx 1.0$ in the turbulent boundary layer, in which more than 20 CVs were placed. A grid convergence study has been performed to test the influence of the grid resolution on the results. Grid dependency study indicated that higher grid resolution in the near-wall region results in negligible changes in the predicted results: the effect of increasing the number of CVs in the wall-normal direction on the predicted mean velocity and Reynolds shear stress profile was at most 1%. Therefore, the simulation results based on the smaller grid (389×280) has been used in the present analysis.

The governing Eqs. 1 - 2 were closed by the RANS based transition model of⁵ using OpenFOAM. The transport equations were discretized on a staggered mesh using finite volume method. The scheme is second order upwind for spatial discretization, and Gauss linear scheme was used to evaluate the gradients. The PIMPLE algorithm was adopted for pressure-velocity coupling, which is a combination of PISO (Pressure Implicit with Splitting of Operator)⁴⁷ and SIMPLEC (Semi-

Implicit Method for Pressure Linked Equations-Consistent)⁴⁸. It should be noted that PIMPLE algorithm can deal with large time steps where the maximum Courant (C) number may consistently be above 1. In this study, the maximum value of C was set consistently equal to 0.6, and OpenFOAM automatically adjusted the time step to achieve the set maximum. In addition, both residuals and distributions of lift and drag coefficients that vary with respect to time (T) were used to track convergence status. The solution fields were iterated until convergence, which required residuals of energy and momentum to drop more than four orders of magnitude, and both lift and drag coefficients almost stopped changing with time. This happened at $T \approx 0.3$, which corresponds to a normalized time $T^* = TU_\infty/c = 6.75$, and similar behavior has been observed by Catalano and Tognaccini⁴⁶ in their numerical study for a low-Reynolds number flow over a SD7003 airfoil at AoA = 10° . Sampling began at $T = 0.6$ (double the time of convergence) and ended at $T = 1.4$, which required approximately 35000 iterations for all simulations.

The fluid was assumed to be air, with freestream turbulence intensity of $Tu = 0.03\%$ and kinematic viscosity of $\nu = 1.5 \times 10^{-5} \text{ m}^2/\text{s}$. Ideally, the value of Tu should be close to zero. From Fig. 3 at the inlet of the domain, the freestream velocity was set equal to 4.5 m/s , which corresponds to $Re_c = 60000$. The chord length was set equal to $c = 0.2 \text{ m}$. At the outlet, a zero-gradient boundary condition was implemented for $\langle U_i \rangle$ ($\langle U \rangle$ for x direction, $\langle V \rangle$ for y direction), k , ω and pressure. At the wall, a no-slip boundary condition was used.

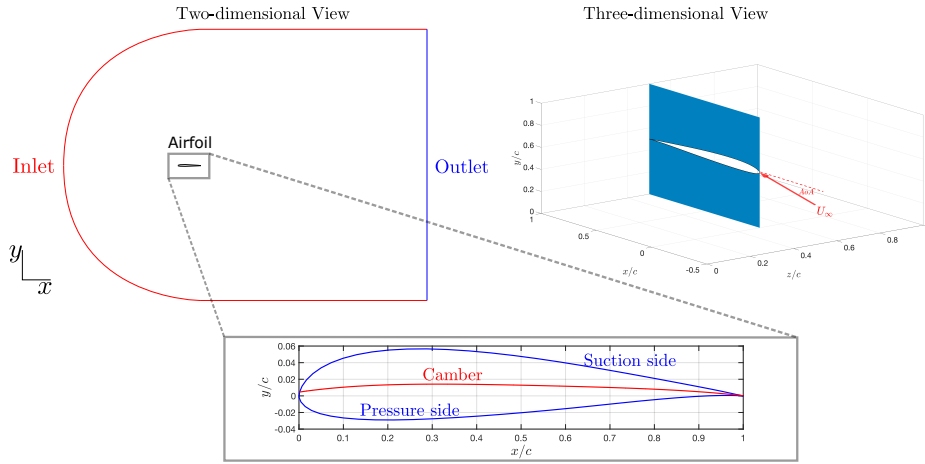


FIG. 3. SD7003 computational domain and boundary conditions: — far field, — outflow, —, and no-slip walls. Depiction of the suction side, camber, and pressure side of the SD7003 airfoil is displayed in the magnified plot. A three-dimensional version of the computational domain is provided with freestream (U_∞) encountering the leading edge at 8° AoA.

IV. REGRESSION MODEL FOR AMPLITUDE PERTURBATION

An important and novel focus of this study is the development of a marker function that modulates the degree of perturbations over the entire flow domain. We have explained earlier that this should lead to better calibrated confidence intervals. In this section, high-order polynomial regressions are constructed using MATLAB software in a least-squares sense to fit both the baseline RANS and in-house DNS datasets. Note that these high-order regressions lay the foundation for the development of the new marker functions.

A. Example: a linear regression

The n^{th} polynomial regression model that describes the relationship between a dependent y and an independent x can be expressed as

$$y(x) = p_1x^n + p_2x^{n-1} + \dots + p_nx + p_{n+1} \quad (19)$$

where $p = 1, \dots, n+1$ stands for the coefficients in descending orders, x is the independent variable. Fig. 4 illustrates a first-order or linear regression model on a random dataset. The errors $y_i - \hat{y}_i$ between the predicted values \hat{y}_i and the actual data values y_i are referred to as residuals. Using MATLAB software, the least-squares method finds the coefficients p_i that best fit this datasets by minimizing the sum of squared residuals, i.e.:

$$RSS = \sum_{j=1}^n (y_j - \hat{y}_j)^2, \quad j = 1, \dots, m \quad (20)$$

where RSS stands for residual sum of squares, y_j is the j th actual value of the dependent variable to be predicted, m represents

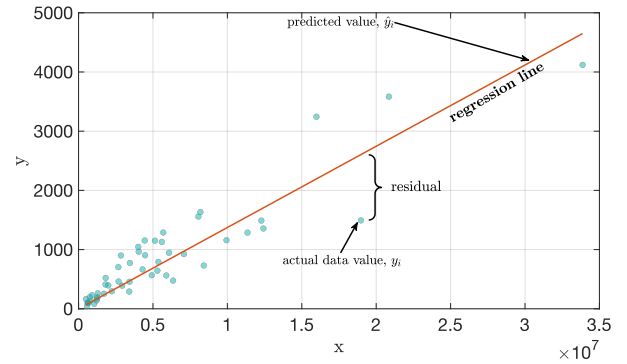


FIG. 4. Linear regression relation between x and y .

TABLE I. Comparison of transition parameters.

Method	X_S/c	X_T/c	X_R/c
SSTLM (Baseline) ⁵	0.03	0.15	0.29
In-house DNS ³⁴	0.02	0.16	0.27
LES ⁴⁹	0.02	0.16	0.27
ILES ⁵⁰	0.03	0.18	0.27

resents the number of points of the datasets, \hat{y}_j is the j th predicted value of y_j .

1. Define untrustworthy regions

To construct marker functions for k^* , first and foremost is to identify the regions where the turbulent viscosity hypothesis becomes invalid. This study identifies the regions where the RANS model gives plausible untrustworthy results based on the comparison between the baseline prediction and the in-house DNS data of³⁴. For the flow over an airfoil geom-

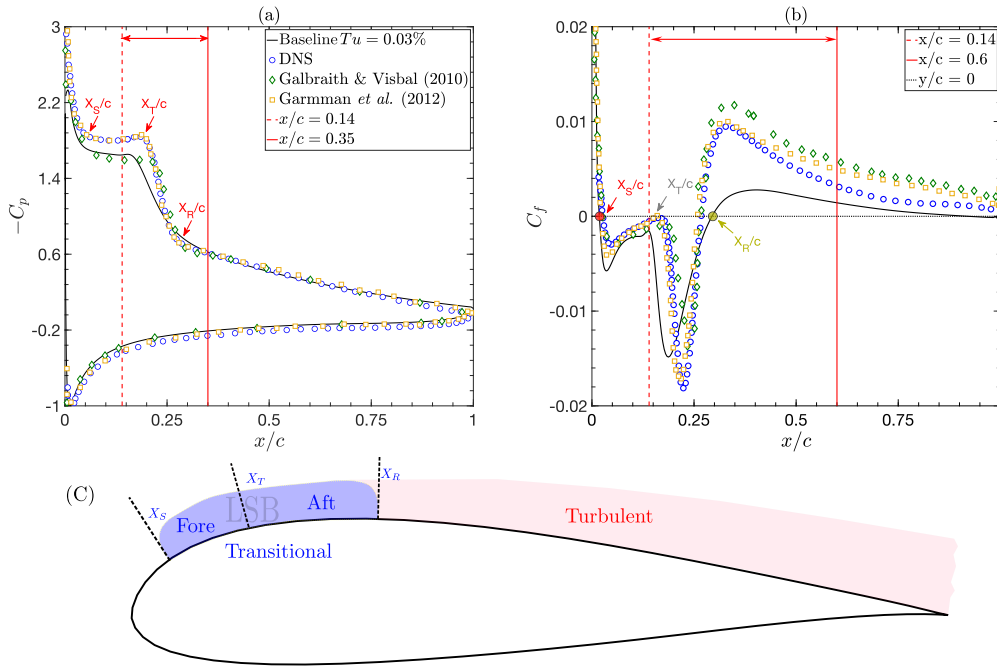


FIG. 5. Distribution of (a) pressure coefficient and (b) skin friction coefficient over the SD7003 airfoil at $Re_c = 6 \times 10^4$ and $AoA = 8^\circ$. Two headed arrow is added to indicate the untrustworthy region. (c) Schematic of transitional and turbulent regions over a SD7003 airfoil with important transitional parameters highlighted.

etry, perhaps the local wall shear stress and the local pressure are the most important parameters, whose dimensionless forms become the skin friction coefficient $C_f = \tau_w / 0.5\rho U_\infty^2$, where τ_w is the wall shear stress, and the pressure coefficient $C_p = (p - p_\infty) / 0.5\rho U_\infty^2$, where p is the undisturbed static pressure and p_∞ is the static pressure in the freestream, respectively. In Figs. 5 (a) and (b), the predicted C_f and C_p are plotted. According to the technique described by Boutilier and Yarusevych⁵¹, Fig. 5 (a) shows three “kinks” as representatives of the separation, transition and reattachment points, denoted X_S/c , X_T/c and X_R/c , respectively. Moreover, the size of the LSB can be determined by finding the X_S/c and X_R/c points, which can be determined as the zeros of the skin friction coefficient⁵². The two methods showed good agreement with each other, and a summary of these important transition parameters are tabulated in Table I. In this study, the LSB is treated to be composed of a “fore” (from X_S/c to X_T/c) and an “aft” (from X_T/c to X_R/c) portion for the sake of analysis simplicity, followed by a fully turbulent region, as shown in Fig. 5 (c). The in-house DNS³⁴ and implicit LES (ILES)/LES data of⁵⁰ and⁴⁹ for C_f and C_p are included for comparison. In the fore portion of the LSB, the predicted C_p profile shows relatively good agreement with the ILES data of⁵⁰, while a clear discrepancy is observed in the aft portion, where it gives a smaller value of C_p , i.e. the region indicated by the two headed arrow. This kind of discrepancy was observed by Tousei *et al.*⁸ in their numerical study as well. Besides, the predicted C_p shows good agreement with the reference data for the turbulent region on the suction side, as well as shows

good agreement with the reference data for the entire pressure side. On the other hand, a noticeable discrepancy is observed on the C_f profile at the negative “trough” in the aft portion of the LSB, as well as at the positive “crest” in the turbulent boundary layer after the reattachment point X_R . In Fig. 5 (b), a shift of the predicted C_f profile in the upstream direction at the trough is observed, and the value of C_f is significantly under-predicted at the crest in the region of turbulent boundary layer for $0.3 < x/c < 0.6$. This behavior has been observed by other researchers as well, e.g., see^{8,46,53}. Therefore, it can be concluded that the region for $0.14 \leq x/c \leq 0.6$, as indicated by the double headed arrow shown in Fig. 5 (b), should be identified as representative for the untrustworthy regions where perturbations should be introduced.

This study ensures that the amplitude perturbation is introduced across the entire boundary layer within the untrustworthy region $0.14 \leq x/c \leq 0.6$, which is further divided into the *ab*, *cd*, *em* and *mf* zone. In Fig. 6, the mean velocity profiles at seven locations downstream of the leading edge are used to illustrate the flow development in the streamwise direction, i.e. *I* = $x/c = 0.1$, *II* = $x/c = 0.15$, *III* = $x/c = 0.2$, *IV* = $x/c = 0.3$, *V* = $x/c = 0.4$, *VI* = $x/c = 0.5$, and *VII* = $x/c = 0.6$. Due to the airfoil curved upper surface, the mean velocity profiles are shifted down to the origin of y/c , denoted $y/c|_o = (y - y_w)/c$ for sake of better contrast, where y_w is the vertical location of the upper surface of the airfoil. Figure 6 clearly shows that the boundary layer thickness increases as the flow develops in the streamwise direction downstream of the leading edge, i.e. the dash line with open circles indicates the approximate thickness of the outer edge of the boundary

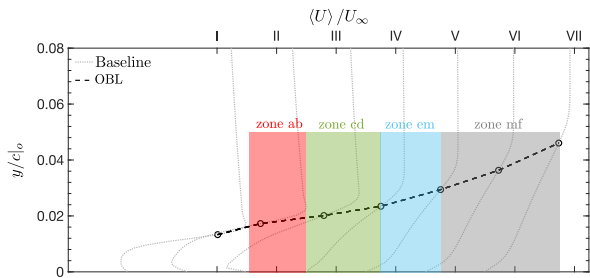


FIG. 6. Injection of uncertainty into the untrustworthy zones: **zone ab**, **zone cd**, **zone em** and **zone mf**. The outer edge of the boundary layer (- - with \circ) at seven locations $I = x/c = 0.02$, $II = x/c = 0.03$, $III = x/c = 0.04$, $IV = x/c = 0.06$, $V = x/c = 0.08$, $VI = x/c = 0.10$, $VII = x/c = 0.12$ (\cdots) selected on the suction side are provided for reference.

layer (OBL). In this study, the regions within which the amplitude perturbation will be introduced are shaded red, green, blue and gray corresponding to the *ab*, *cd*, *em* and *mf* zone, respectively, as shown in Fig. 6. It is clear that all these shaded regions extend well beyond OBL, i.e. $0 < y/c|_o < 0.05$, implying the propagation of the amplitude perturbation effect deeper into the outer boundary layer as the flow develops further downstream of the leading edge.

2. Polynomial regression for DNS/RANS turbulence kinetic energy datasets

In this study, MATLAB software was used to construct a set of least squares higher-order regression lines that are used to fit seventh-order polynomials to both the baseline RANS and in-house DNS datasets, i.e. gray lines with open circles, for turbulence kinetic energy normalized with the freestream velocity squared, k/U_∞^2 are shown in Figs. 7 (a) and (b). There are 5 locations selected for the *ab* zone and 12 locations for the *cd* zone. The regression based k/U_∞^2 profiles for the *ab* and *cd* zone are colored red and green, respectively, with a uniform spacing of $x/c = 0.01$. As the flow proceeds further downstream, the regression based k/U_∞^2 profiles for the *ef* zone, which comprises a *em* and *mf* subzone, are colored blue, within which 15 locations are selected with a uniform spacing of $x/c = 0.02$. Within each zone same number of locations are selected for both the regression based RANS and in-house DNS k/U_∞^2 profiles, as documented in Table II. As a result, a total of 32 locations are selected and placed uniformly on the suction side of the airfoil, ranging from the LSB to the fully turbulent flow further downstream. In addition, the locations are more densely packed by imposing a smaller spacing distance within the *ab* and *cd* zone, where the LSB evolves and complex flow features start developing. Therefore, a closer investigation into this region is taken. From Figs. 7 (a) and (b), the regression based RANS k/U_∞^2 profiles in general exhibit a similar behavior as that for in-house DNS, i.e. a gradual increase of the k/U_∞^2 profile in the *ab* and *cd* zone, followed by a reduction of the profile further down-

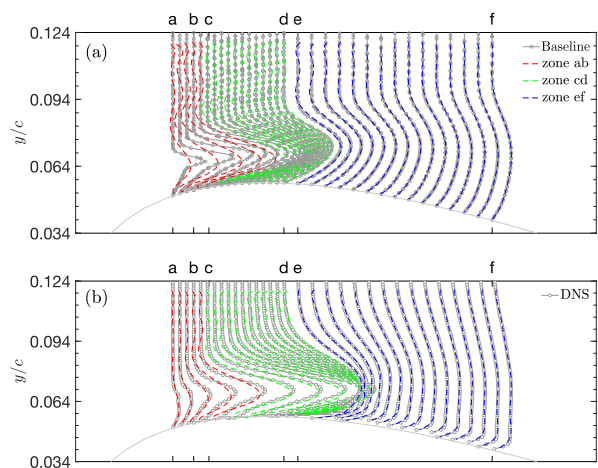


FIG. 7. (a) Regressed profile of normalized turbulence kinetic energy for the baseline RANS and (b) in-house DNS datasets (gray profiles) along the suction side of the SD7003 airfoil (geometry depicted by gray line): from left to right are **zone ab**, **zone cd** and **zone ef**.

stream in the *ef* zone.

3. Spatial discrepancies in k/U_∞^2 regressions from DNS/RANS comparison

In Figs. 8 (a) and (b), these 32 regression based k/U_∞^2 profiles are shifted to the origin of the x/c and y/c axes, respectively, for sake of strong contrast. The baseline predictions and the in-house DNS data are also included for reference, depicted by the gray lines with open circles and shifted to the origin of the x/c axis to be distinguished from these regression based profiles. From Fig. 8 (a), the regression based RANS k/U_∞^2 profiles increase in magnitude as the flow moves further downstream. This is qualitatively similar to that for the in-house DNS profile shown in Fig. 8 (b). From Figs. 8 (a) and (b), the regression based RANS k/U_∞^2 profiles increase in a somewhat larger magnitude than that for in-house DNS for the *ab* zone; however, they are significantly reduced in magnitude compared to that for in-house DNS for the *cd* zone (in the aft portion of the LSB), i.e., the magnitude of reduction is around 50%. For the *ef* zone, both the regression based RANS and in-house DNS k/U_∞^2 profiles show a gradual decrease in magnitude as the flow moves further downstream. Overall, the regression based RANS and in-house DNS k/U_∞^2 profiles are similar in magnitude for the *ab* and *ef* zones, but the discrepancy is significant in the aft portion of the LSB for the *cd* zone.

4. Marker for k^*

As noted earlier relatively few methods thus far have been developed to construct marker functions, e.g., see⁹ and³³. Essentially, they can be classified into two categories: (1) spatially varying magnitude of Δ_B and (2) identifying regions that

TABLE II. Zone ranges for the untrustworthy region.

	zone <i>ab</i>	zone <i>cd</i>	zone <i>em</i>	zone <i>mf</i>
x/c	$0.14 \leq \frac{x}{c} \leq 0.18$	$0.18 < \frac{x}{c} \leq 0.3$	$0.3 < \frac{x}{c} \leq 0.4$	$0.4 < \frac{x}{c} \leq 0.6$
y/c	$y_w \leq \frac{y}{c} \leq 0.1$	$y_w \leq \frac{y}{c} \leq 0.1$	$y_w \leq \frac{y}{c} \leq 0.1$	$y_w \leq \frac{y}{c} \leq 0.1$
Number of locations	5	12	15	
Spacing of x/c	0.01		0.02	

deviate from parallel shear flow. All of these methods essentially use only one explanatory variable to predict the error in RANS model predictions. In this study, a novel method based on least squares high-order regressions is developed to construct a switch marker function for k^* . This method uses a set of explanatory variables dedicated to the identified untrustworthy zones, which aims at introducing correct level of uncertainty by strictly comparing the RANS predictions for turbulence kinetic energy to the in-house DNS data.

We performed numerous tests and found that increasing the order of polynomial regressions higher than seven no longer gave more accurate results. Consequently, the seventh-order polynomial regression lines for the k/U_∞^2 profiles were conducted, as shown in Fig. 9. For each of the *ab*, *cd* and *ef* zone, the averaged regression relations for both RANS and in-house DNS are computed using the equation defined as follows:

$$k_{RANS/DNS}^{ave}|_{zone\ ab/cd/ef} = \frac{\sum_{i=1}^n P_i(\frac{y}{c}|_o)}{n}, \quad (21)$$

where i represents the i th location on the suction side of the SD7003 airfoil (there are 32 selected locations), P_i represents the polynomial regression at the i th location, and n is the number of locations for each zone, as summarized in Table II.

The regression based k/U_∞^2 profiles for the *ab*, *cd* and *ef* zone are plotted in Figs. 9 (a), (b) and (c), respectively. The two solid lines with filled markers represent the mean of the regression based datasets for both RANS and in-house DNS. In each zone, Figs. 9 (a), (b) and (c) clearly show the discrepancy between these two averaged regression relations. For the *ab* zone, Fig. 9 (a) shows a small discrepancy close to zero at the wall, i.e. $y/c|_o = 0$, as well as in the far outer region, i.e. $y/c|_o > 0.025$. Besides, the discrepancy tends to increase with $y/c|_o$ and peaks around $y/c|_o = 0.015$. Within the *cd* zone shown in Fig. 9 (b), there is a large discrepancy at the wall and the discrepancy retains at a nearly consistent level until peaks around $y/c|_o = 0.015$, then gradually decreases with $y/c|_o$ to approach the value of zero. It is interesting that the discrepancy peaks around $y/c|_o = 0.15$ for both the *ab* and *cd* zone (aft portion of the LSB). On the other hand, a relatively small discrepancy is observed consistently throughout the entire boundary layer for the *ef* zone, as shown in Fig. 9 (c). This indicates that the RANS based transition model⁵ tends to become more trustworthy in the predictions for the turbulence kinetic energy in the far downstream region than that within/close to the LSB, i.e. the *ab* and *cd* zone. From Figs. 9 (a), (b) and (c), the discrepancy between the averaged regression relations for RANS and in-house DNS describes

the degree of untrustworthiness in the $y/c|_o$ direction ranging from the *ab* zone to the *ef* zone across the suction side, therefore the discrepancy can be used as an approximation to a marker function. This study defines a correction factor based on the k/U_∞^2 discrepancy between the regression based RANS and in-house DNS, which can be written as follows:

$$CF_k = \left| \frac{\text{Averaged DNS}}{\text{Averaged SSTLM}} \right|. \quad (22)$$

Equation 22 indicates that CF_k is constantly positive, which satisfies the physical realizability constraint, i.e. $k^* \geq 0$. For each zone, the discrepancy data obtained using Eq. 22 are depicted by the blue solid circles, as shown in Figs. 10 (a), (b) and (c). Using MATLAB software, the marker function for each zone can be constructed by fitting to the corresponding CF_k data, i.e., fitting a seventh-order polynomial to the discrepancy data for the *ab* and *ef* zone, while fitting a Fourier series to the discrepancy data for the *cd* zone, as shown in Figs. 10 (a), (c), and (b), respectively.

Therefore, a switch marker function that introduces local injection of perturbation with respect to the *ab*, *cd* and *ef* zone can be written as follows:

$$\text{Switch } M_k = \begin{cases} a_0^{ab} \left(\frac{y-y_w^{ab}}{c}\right)^7 + a_1^{ab} \left(\frac{y-y_w^{ab}}{c}\right)^6 + \dots + \\ a_5^{ab} \left(\frac{y-y_w^{ab}}{c}\right)^2 + a_6^{ab} \left(\frac{y-y_w^{ab}}{c}\right) + a_7^{ab} & \text{if zone } ab, \\ a_0^{cd} + a_1^{cd} \cos\left(w \left(\frac{y-y_w^{cd}}{c}\right)\right) + \\ b_1^{cd} \sin\left(w \left(\frac{y-y_w^{cd}}{c}\right)\right) + \\ + a_2^{cd} \cos\left(\left(2w \left(\frac{y-y_w^{cd}}{c}\right)\right)\right) + & \text{if zone } cd, \\ b_2^{cd} \sin\left(\left(2w \left(\frac{y-y_w^{cd}}{c}\right)\right)\right) \\ a_0^{em} \left(\frac{y-y_w^{em}}{c}\right)^7 + a_1^{em} \left(\frac{y-y_w^{em}}{c}\right)^6 + \dots + \\ a_5^{em} \left(\frac{y-y_w^{em}}{c}\right)^2 + a_6^{em} \left(\frac{y-y_w^{em}}{c}\right) + a_7^{em} & \text{if zone } em, \\ 2.8 & \text{if zone } mf, \end{cases} \quad (23)$$

where $a_0, a_1, a_2, a_3, a_4, a_5, a_6, a_7$ represent the polynomial coefficients; $a_0, a_1, b_1, a_2, b_2, w$ represent the Fourier coefficients. Therefore, the perturbed turbulence kinetic energy, k^* , is defined as follows:

$$k^* = kM_k. \quad (24)$$

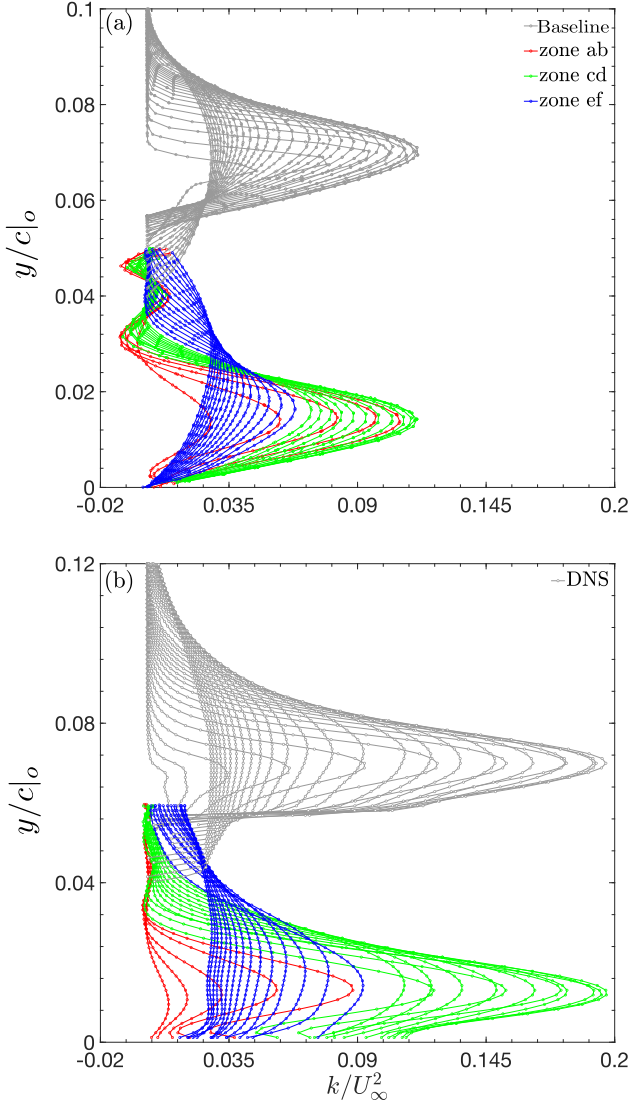


FIG. 8. (a) Regressed profile of normalized turbulence kinetic energy for baseline RANS and (b) in-house DNS for *zone ab*, *zone cd* and *zone ef*. Actual datasets (gray profiles) for baseline RANS and in-house DNS are provided for reference.

It is worth noting that the development of spatial variations in M_k , are what the turbulence machine learning efforts are focused on. Because when a neural network model is developed to predict the perturbation in the flow, this neural network model will not predict the same perturbation at all points in the flow domain. Instead, it will naturally lead to a non-uniform perturbation. The key differences between my work and the work based on machine learning is two pronged: (1) the choice of the model and (2) the choice of the modeling basis (or the explanatory variables utilized to predict the perturbation). We have used a seventh-order regression, the work based on machine learning uses a random forest or neural network. We have utilized a small set of explanatory variables in M_k that is developed based on physics arguments and prior ex-

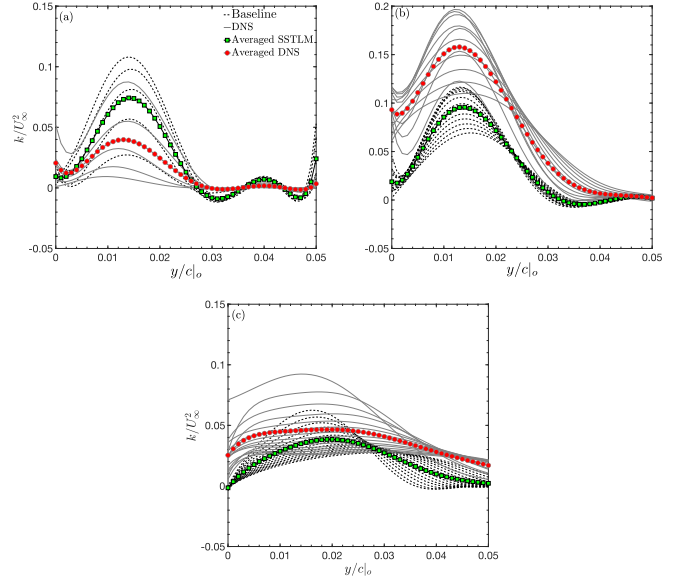


FIG. 9. Mean of regression lines for normalized turbulence kinetic energy of both baseline RANS (line with green squares) and in-house DNS (line with red circles). (a) *zone ab*; (b) *zone cd*; and (c) *zone ef*. Also included are profiles of baseline RANS (gray-dashed) and in-house DNS (gray-solid) for reference.

perience. The work based on machine learning utilize a large set of explanatory variables (called features) that is almost 100 in number and includes invariants of the mean velocity field, scaled distance from the wall.

If a uniform value of M_k is used, then Eq. 24 becomes

$$k^* = k\Delta_k, \quad (25)$$

where k is the perturbed turbulence kinetic energy from the previous time step, and Δ_k represents a uniform value of M_k . The value of Δ_k must be larger than zero to satisfy physical realizability. Due to airfoil curved surfaces, y_w varies along the suction side. If let $y_w = f(x)$ represent the curved upper surface, then its gradient can be calculated by taking the derivative of $f(x)$, e.g., $df(x)/dx$. In Eq. 23, the strategy to choose a reasonable magnitude for y_w as representative of a zone is to find the minimum value of y_w , which ensures that the realizability constraint of $M_k \geq 0$ is satisfied, and hence $k^* \geq 0$. Note that the value of $df(x)/dx$ approaches to the value of zero around $x/c = 0.266$, i.e. sitting within the *cd* zone. This implies that the minimum value of y_w is located closer to the leading edge for $x/c < 0.266$, while the minimum value of y_w is located closer to the trailing edge for $x/c > 0.266$.

As noted earlier in Fig. 6, the *ef* zone is composed of two subzones, i.e. *em* and *mf*, as illustrated in Fig. 11. Figure 11 enlarges the *ef* zone, in which the regression based k/U_∞^2 profiles for both RANS and in-house DNS are shifted down to the origin of y , to highlight the discrepancy in the region for $0.3 < x/c < 0.6$, within which the profiles for the *em* subzone are painted blue, while the profiles are painted gray for the *mf* subzone. It is clear that a similar level of discrepancy between

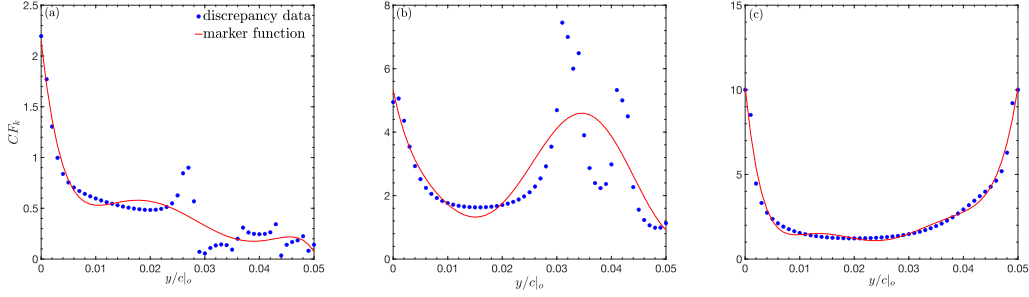


FIG. 10. Defining the marker function for (a) zone *ab*, (b) zone *cd* and (c) zone *ef* based on the corresponding discrepancy data.

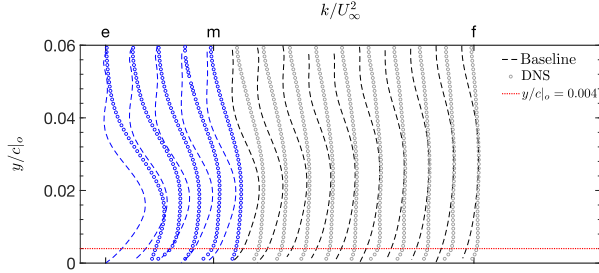


FIG. 11. Defining the marker function for subzone *mf*.

the regression based RANS and in-house DNS profile across the *mf* subzone is observed, as shown in Fig. 11. From Fig. 11, the discrepancy is significant in the vicinity of the wall, i.e at $y/c|_o = 0.004$, which corresponds to an approximate value of 2.8 for CF_k in Fig. 10 (c). For sake of simplicity, the uniform value of 2.8 for M_k is employed for the *mf* subzone in Eq. 23.

We visualize the spatial variation of the magnitude of M_k from the contours of $0 < M_k < 1$ and $1 < M_k < 10$, as shown in Figs. 12 (a) and (b), respectively. From Fig. 12 (a), it is clear that the magnitude of $0 < M_k < 1$ is more prevalent in the *ab* zone, and in the upper portion of the *cd* zone. In Fig. 12 (a), an overall decreasing trend of M_k in magnitude with y/c is observed for the *ab* zone. On the other hand, the M_k magnitude for both the *cd* and *em* zone varies with y/c in a fashion consistent with the behavior observed in Figs. 10 (b) and (c). Moreover, a uniform magnitude of M_k is observed for the *ef* zone, which confirms the uniform magnitude of 2.8.

V. RESULTS AND DISCUSSION

A. Sensitivity to Δ_k

1. Skin friction coefficient

A set of C_f distributions undergoing the Δ_k perturbations are shown in Fig. 13. The baseline prediction for C_f is used as a reference. The increasing magnitude of Δ_k is indicated by lighter to darker hues, as shown in Fig. 13. In addition, the red solid arrows are added to indicate the trend of C_f with increasing Δ_k , and the regions that contain a peak negative (trough) and a peak positive (crest) value of C_f are enlarged to distinguish the clusters of C_f profiles. In Fig. 13, the magnitude of C_f profiles increases with Δ_k perturbations for $\Delta_k < 1$ ($\Delta_k = \{0.1, 0.25, 0.5, 0.75\}$) and $\Delta_k > 1$ ($\Delta_k = \{2, 4, 6, 8\}$), respectively, at the trough (around X_T), indicating a monotonic increase. As the flow moves further downstream within the aft portion of the LSB, the magnitude of C_f tends to decrease monotonically when the value of Δ_k is increased; as the flow proceeds further downstream of X_R , a monotonic increase with Δ_k in the magnitude of C_f again occurred for $\Delta_k < 1$ and $\Delta_k > 1$. It should be noted that the C_f profiles tend to converge and collapse onto a single curve when Δ_k is increased. The

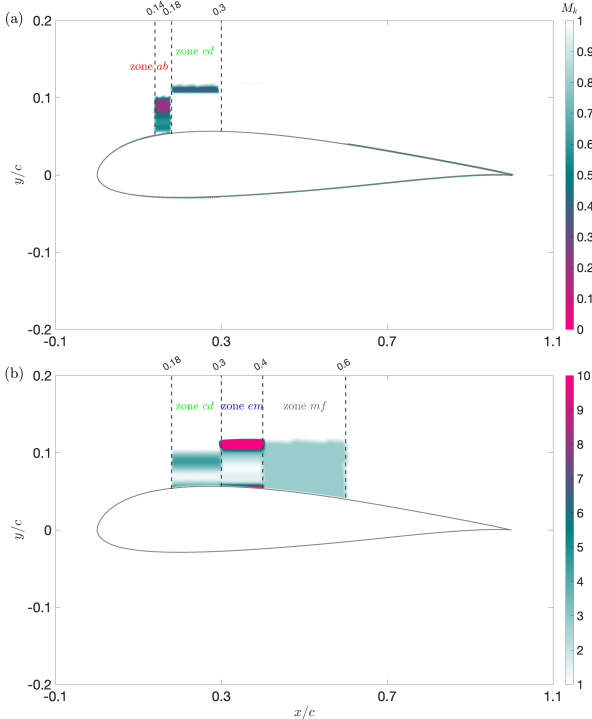


FIG. 12. Contours of M_k (Eq. 23) for (a) $0 < M_k < 1$ and (b) $1 < M_k < 10$ in an *xy* plane. The dashed lines in (a) and (b) denote the actual locations on the suction side of the airfoil, which separate the *ab*, *cd*, *em* and *mf* zone.

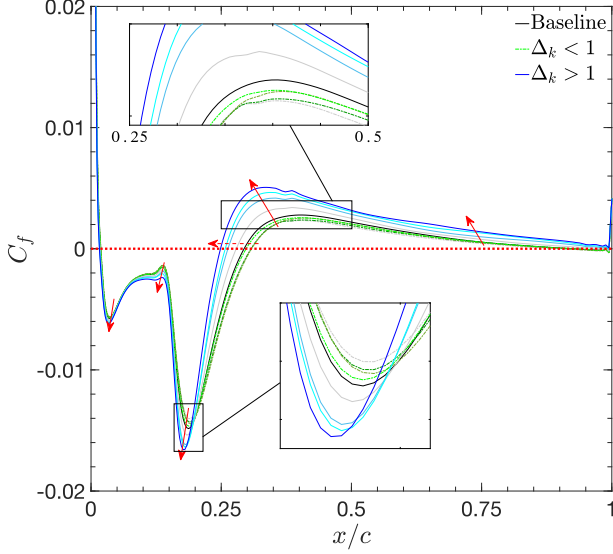


FIG. 13. Skin friction coefficient distributions over the suction side of the airfoil with enlarged regions at the trough and the crest. Displayed are k^* perturbations with uniform Δ_k : $\Delta_k < 1$ ($\Delta_k = \{0.1, 0.25, 0.5, 0.75\}$) and $\Delta_k > 1$ ($\Delta_k = \{2, 4, 6, 8\}$); increasing values indicated by lighter to darker hues. Red solid arrows (\rightarrow) are provided to indicate increasing magnitude of C_f with Δ_k ; the red dashed arrow (\leftrightarrow) is provided to indicate the shift in reattachment point with Δ_k . Note that the value of Δ_k must be larger than zero to satisfy realizability. The baseline prediction is provided for reference.

baseline prediction is well enveloped in between the $\Delta_k < 1$ and $\Delta_k > 1$ perturbations. Compared to the baseline prediction, rather subtle increases in the magnitude of C_f for $\Delta_k < 1$ is observed, as contrasted with more noticeable increases in C_f for $\Delta_k > 1$. This indicates that the simulation's response to the injection of Δ_k is more dependent on $\Delta_k > 1$ than $\Delta_k < 1$. This behavior is highlighted in the enlarged trough and crest region. In addition, the dashed red arrow is added along the line of zeros of C_f to indicate the tendency of a shift of X_R in the upstream direction when the value of Δ_k is increased for both $\Delta_k < 1$ and $\Delta_k > 1$.

Since wall shear stress is a consequence of momentum transfer from the mean flow to the wall surface⁵⁴, the magnitude of mean velocity is closely related to the magnitude of C_f . In the aft portion of the LSB, the $\Delta_k > 1$ perturbations overall yield a smaller magnitude of C_f , and an increase in the magnitude of mean velocity is expected, while the opposite is true for the $\Delta_k < 1$ perturbations.

2. Mean velocity field

Contours of the mean velocity normalized with the free stream velocity, $\langle U \rangle / U_\infty$ from the baseline, Δ_k perturbations, and in-house DNS of³⁴ in an xy plane are shown in Fig. 14. The streamlines for depicting a large recirculation vortex within the LSB, characterized by the region of reverse flow

($\langle U \rangle / U_\infty < 0$)⁵⁵, are included as well. This large recirculating region contains large-scale events (coherent structures), which are at low-frequency fluctuations due to very-large scale of unsteadiness of the recirculating region itself⁵⁶. As a consequence, the $\langle U \rangle / U_\infty$ contours exhibit a LSB surviving after time-averaging, as shown in Fig. 14. This behavior has been observed in the experimental measurements of⁵⁷, RANS analysis of⁴⁶, and ILES/LES data of⁵⁰ and⁴⁹. Figure 14 clearly shows that the baseline prediction for the LSB shows a comparable length to in-house DNS; however, the LSB's height is under-predicted. This inaccurate prediction for the LSB height alters the effective shape of the airfoil, hence inaccuracy in simulation results^{58,59}. This reflects the error in RANS model predictions in the region of the LSB. Compared to the baseline prediction, rather subtle responses to the $\Delta_k < 1$ perturbations ($\Delta_k = 0.1, 0.25, 0.5$) are observed, which confirms the behavior shown in Fig. 13. On the other hand, more noticeable changes are observed with the $\Delta_k > 1$ perturbations ($\Delta_k = 4, 6, 8$), i.e., a clear suppression of the LSB length; in addition, it is clear that the magnitude of mean velocity increases downstream of the LSB within the attached turbulent boundary layer, characterized by the more clustered streamlines compared to the baseline prediction. This confirms the reduction in the magnitude of the LSB, as shown in Fig. 13. There are two monotonic behaviors: first, the size of the recirculating region decreases monotonically with Δ_k (shallower region of streamlines), showing a tendency of deviating from the in-house DNS contour; second, the magnitude of $\langle U \rangle / U_\infty$ monotonically increases with Δ_k in the attached turbulent boundary layer (more densely clustered streamlines), showing a tendency of approaching closer to the in-house DNS contour.

3. Reynolds shear stress

Contours of the Reynolds shear stress normalized with the freestream velocity squared, $-\langle u_1 u_2 \rangle / U_\infty^2$ from the baseline, Δ_k perturbations, and in-house DNS of³⁴ in an xy plane are presented in Fig. 15. Also included are the streamlines for the depiction of the recirculation vortex region. From Fig. 15, all of the $-\langle u_1 u_2 \rangle / U_\infty^2$ contour plots show a magnitude of nearly zero in the region near the leading edge and in the outer region of the flow, and a peak is found within the LSB around X_T , i.e., the bright yellow region, from which the magnitude of $-\langle u_1 u_2 \rangle / U_\infty^2$ reduces as the flow moves further downstream. A similar behavior was also observed by Zhang and Rival⁵⁷ in their experimental measurements. Overall, the baseline prediction for Reynolds shear stress gives a smaller value than the in-house DNS data, especially in the LSB. It should be noted that the contour plots of $-\langle u_1 u_2 \rangle / U_\infty^2$ and $\langle U \rangle / U_\infty$ show a similar trend: a lack of sensitivity to the $\Delta_k < 1$ ($\Delta_k = 0.1, 0.25, 0.5$) perturbations, while a rather strong sensitivity to the $\Delta_k > 1$ ($\Delta_k = 4, 6, 8$) perturbations in both the transitional and turbulent region. In general, the Reynolds shear stress contour exhibits a larger response to Δ_k compared to the mean velocity contour. From Fig. 15, the $\Delta_k < 1$ perturbations give a somewhat larger value of $-\langle u_1 u_2 \rangle / U_\infty^2$ than the base-

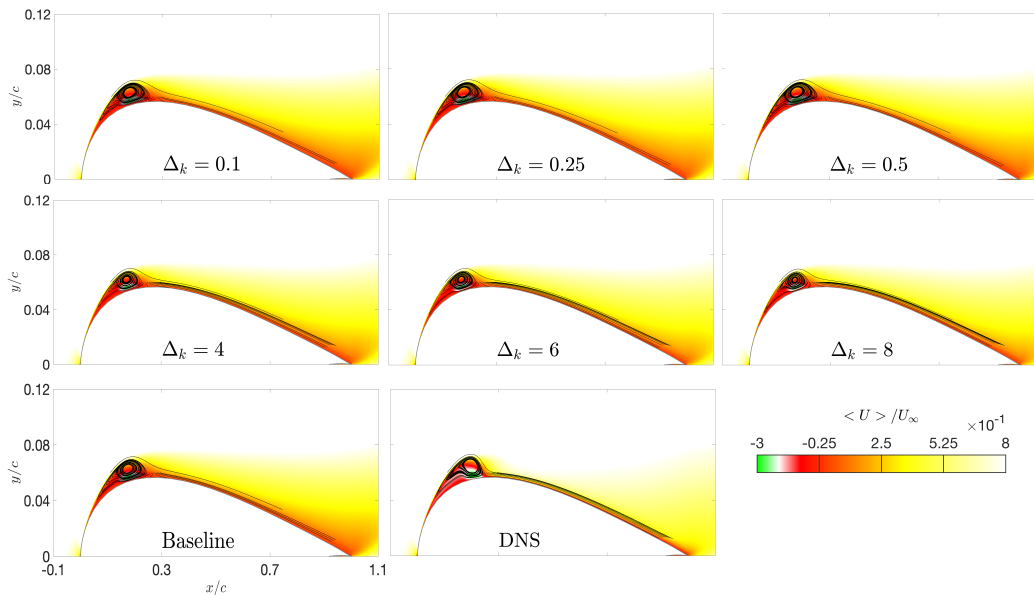


FIG. 14. Contours of $\langle U \rangle / U_\infty$ with different values of Δ_k : $\Delta_k < 1$ ($\Delta_k = \{0.1, 0.25, 0.5\}$) and $\Delta_k > 1$ ($\Delta_k = \{4, 6, 8\}$) in an xy plane. Baseline prediction is provided for reference, and in-house DNS data are included for comparison. Streamlines show the size of the LSB on the suction side of the airfoil.

line prediction, while the $\Delta_k > 1$ perturbations do the opposite. In addition, the $\Delta_k < 1$ perturbations slightly reduce the magnitude of $-\langle u_1 u_2 \rangle / U_\infty^2$ when the value of Δ_k is increased, as opposed to the $\Delta_k > 1$ perturbations, which greatly reduces the magnitude of $-\langle u_1 u_2 \rangle / U_\infty^2$. In addition, it is clear that the peak value for $-\langle u_1 u_2 \rangle / U_\infty^2$ gradually becomes smaller as the value of Δ_k is increased, in particular for $\Delta_k > 1$. This is accompanied with a suppression of the recirculating region and hence a decrease in the turbulence kinetic energy⁶⁰. In Fig. 15, the $\Delta_k > 1$ perturbations tend to approach closer to the in-house DNS data in the turbulent boundary layer, while the $\Delta_k < 1$ perturbations tend to result in a closer agreement with the in-house DNS data in the LSB. According to Davide *et al.*⁶⁰, the overall turbulence kinetic energy can be decomposed into the large-scale coherent (Kelvin-Helmholtz induced) and stochastic (turbulence-induced) contributions. With the total energy in the mean flow remained constant, the Δ_k perturbations in a sense redistribute the Reynolds-shear-stress momentum transfer between turbulence and mean flow.

B. Comparison between uniform Δ_k and M_k

1. Skin friction coefficient and pressure coefficient

Distributions of the skin friction coefficient and the pressure coefficient, C_f and C_p , are shown in Figs. 16 (a) and (b). The in-house DNS³⁴ and ILES/LES data of⁵⁰ and⁴⁹ are included for comparison. In Figs. 16 (a) and (b), an enveloping behavior with respect to the baseline prediction is observed. Figure 16 (a) shows that the effect of M_k is more prevalent in the aft portion of the LSB $0.25 < x/c < 0.28$, as well as in the

region downstream of the LSB $0.28 < x/c < 0.6$. This reflects the effect of spatial variability in M_k . In addition, the uncertainty bound generated from the M_k perturbation sits within the gray envelope of $\Delta_k = 8$. Figure 16 (a) clearly shows that the uncertainty bound generated from the M_k perturbation is well encompassed by the uniform $\Delta_k = 0.1$ and $\Delta_k = 8$ perturbations. It is interesting to note that the $\Delta_k = 8$ perturbation overall tends to approach closer to the in-house DNS³⁴ and ILES/LES data of⁵⁰ and⁴⁹ than the $\Delta_k = 0.1$ perturbation does. At the trough shown in Fig. 16 (a), the $\Delta_k = 8$ perturbation gives a larger magnitude of C_f , sitting below the baseline prediction and showing a clear tendency to approach closer to the in-house DNS³⁴ and LES⁴⁹ data. In addition, Fig. 16 (a) clearly shows that the reattachment point is well encompassed by the $\Delta_k = 8$ perturbation. Further downstream of reattachment point, the uncertainty bound generated from both the $\Delta_k = 8$ and M_k perturbations show a tendency to approach closer to the in-house DNS³⁴ and the ILES/LES data of⁵⁰ and⁴⁹, while the $\Delta_k = 0.1$ perturbation under-predicts the baseline prediction and deviates from the reference data.

At the flat spot and the kink (X_R) followed by a steep drop on the C_p profile, the uncertainty bound generated from the M_k perturbation is encompassed by the $\Delta_k = 8$ perturbation, as shown in the enlarged regions in Fig 16 (b). In addition, a tendency for the $\Delta_k = 8$ and M_k perturbations to approach closer to the in-house DNS³⁴ and LES data of⁴⁹ is observed at the flat spot and the kink. On the other hand, it is interesting that the $\Delta_k = 0.1$ perturbation shows a tendency of approaching toward the ILES data of⁵⁰ in the enlarged regions shown in Fig. 16 (b). In the region downstream of the kink and along the entire pressure side, both $\Delta_k = 0.1$ and $\Delta_k = 8$ perturbations are almost negligible in magnitude, i.e., a collapse onto

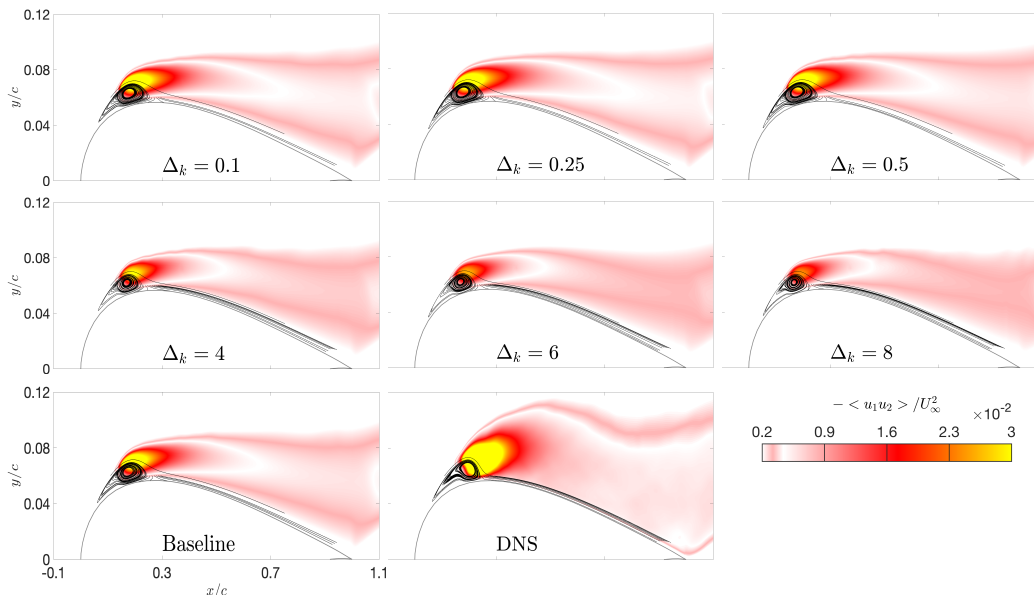


FIG. 15. Contours of $-\langle u_1 u_2 \rangle / U_\infty^2$ with different values of Δ_k : $\Delta_k < 1$ ($\Delta_k = \{0.1, 0.25, 0.5\}$) and $\Delta_k > 1$ ($\Delta_k = \{4, 6, 8\}$) in an xy plane. Baseline prediction is provided for reference, and in-house DNS data are included for comparison. Streamlines show the size of the LSB on the suction side of the airfoil.

the baseline prediction. It should be noted that the baseline prediction overall shows good agreement with the in-house DNS data³⁴ and ILES/LES data of⁵⁰ and⁴⁹, especially good agreement with the ILES/LES data of⁵⁰ and⁴⁹ for the pressure side. This indicates a low level of the model form uncertainty in the predictions for C_p for these regions.

2. Mean velocity field

The $\langle U \rangle / U_\infty$ profiles across the entire boundary layer on the suction side of the airfoil are plotted in Fig. 17. Overall, the baseline prediction at each location is encompassed by the $\Delta_k = 0.1$ and $\Delta_k = 8$ perturbations, exhibiting an enveloping behavior, as shown in Fig. 17. The baseline prediction for the $\langle U \rangle / U_\infty$ profile at $x/c = 0.15$ (X_T) matches the in-house DNS profile of³⁴, except in the regions $y/c|_o < 0.007$ (next to the wall) and $y/c|_o > 0.011$ (upper portion of the boundary layer), where it gives slightly smaller values of $\langle U \rangle / U_\infty$, as shown in Fig. 17. At $x/c = 0.2$ (in the aft portion of the LSB), the baseline prediction for the $\langle U \rangle / U_\infty$ profile shows good agreement with the in-house DNS profile in the region of reverse flow $y/c|_o < 0.011$, with a somewhat reduction in the predicted $\langle U \rangle / U_\infty$ profile in the upper portion of the boundary layer $0.011 < y/c|_o < 0.027$. For the attached turbulent boundary layer, the baseline predictions for the $\langle U \rangle / U_\infty$ profiles at $x/c = 0.3$, $x/c = 0.4$ and $x/c = 0.5$ give smaller values of $\langle U \rangle / U_\infty$ compared to the in-house DNS profiles, and the discrepancies are comparable with each other.

Figure 17 shows that the $\Delta_k = 0.1$ perturbation under-predicts the baseline prediction, and the simulation's response to the $\Delta_k = 0.1$ perturbation is negligibly small within both

the transitional and turbulent boundary layer. This well confirms the behavior of the $\Delta_k = 0.1$ perturbation in the prediction for C_f , as shown in Fig. 16 (a). As the flow proceeds downstream from $x/c = 0.15$ to $x/c = 0.3$, the uncertainty bounds generated from the $\Delta_k = 0.1$ perturbations gradually increase in size, although the increase is rather subtle. This confirms the slightly increased C_f in magnitude compared to the baseline prediction for the aft portion of the LSB. As the flow moves further downstream from $x/c = 0.4$ to $x/c = 0.5$ (in the attached turbulent boundary layer), the $\Delta_k = 0.1$ perturbation gradually reduces the size of the uncertainty bounds at a decreasing rate, reflecting the damping effect of the positive values of C_f on the mean flow.

On the other hand, the $\Delta_k = 8$ perturbation over-predicts the baseline prediction, exhibiting rather noticeable uncertainty bounds, as shown in Fig. 17. As the flow proceeds from $x/c = 0.15$ to $x/c = 0.3$, it is interesting to note that the uncertainty bounds generated from the $\Delta_k = 8$ perturbations increase blatantly in size, showing a tendency of approaching closer to the in-house DNS data. In addition, the effect of the $\Delta_k = 8$ perturbation tends to become more prevalent in the near-wall region, which well confirms the significantly reduced C_f in magnitude compared to the baseline prediction for $0.15 < x/c < 0.3$, as shown in Fig. 16 (a). As the flow proceeds further downstream from $x/c = 0.4$ to $x/c = 0.5$, the uncertainty bounds become larger in the upper section of the mean velocity profiles, while remain at a relatively small magnitude in the near-wall region due to the large positive values of C_f at the crest shown in Fig. 16 (a), reflecting the weakening propagation of the effect of the positive C_f values deeper into the outer boundary layer.

Unlike the $\Delta_k = 0.1$ and $\Delta_k = 8$ perturbation, M_k identi-

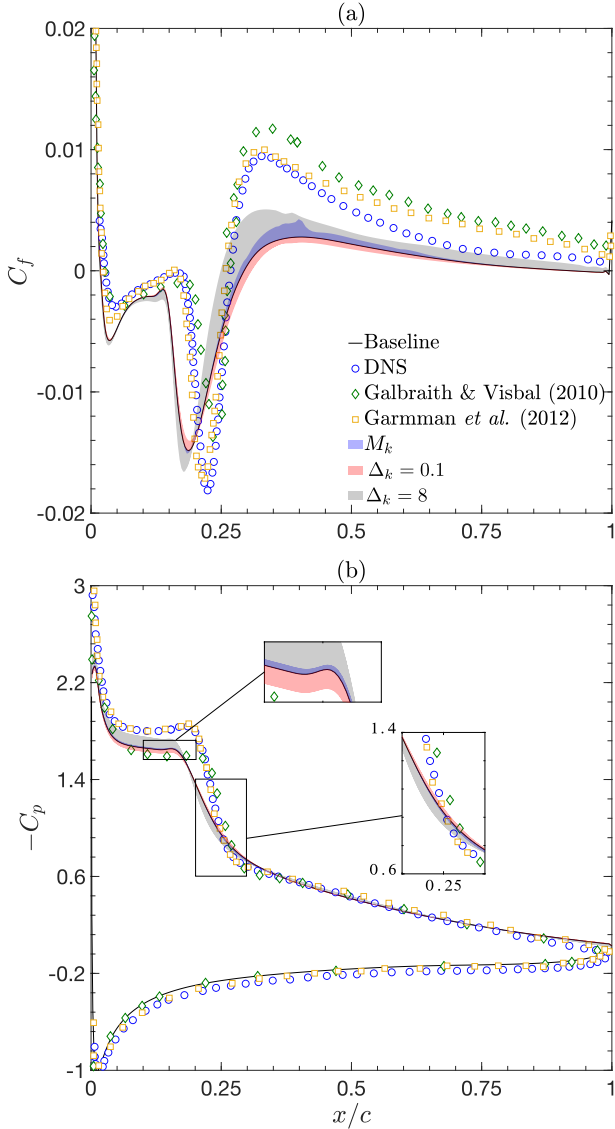


FIG. 16. (a) Profile of skin friction coefficient and (b) pressure coefficient with enlarged regions at the flat spot and the kink. Displayed are envelopes for uniform k^* perturbations: $\Delta_k = 0.1$ (red envelope), $\Delta_k = 8$ (gray envelope), and M_k (blue envelope). The baseline prediction is provided for reference. \circ in-house DNS data³⁴.

fies the untrustworthy regions in which uncertainty will be injected. In Fig. 17, the uncertainty bounds generated from the M_k perturbations in general over-predict the baseline prediction, and sit within the uncertainty bounds generated from the $\Delta_k = 8$ perturbations. It should be noted that the sole effect of the M_k perturbation on the predicted mean velocity profile is rather small. In section V C, the M_k perturbation is compounded with the eigenvalue perturbation (1c, 2c, 3c) to construct more effective uncertainty bounds.

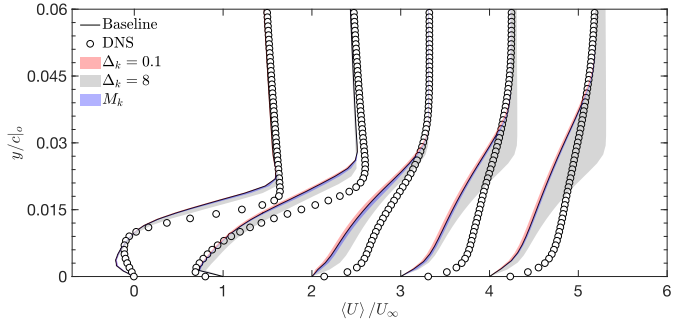


FIG. 17. Streamwise mean velocity profiles in the aft portion of the LSB ($x/c = 0.15$ and 0.2) and in the attached TBL ($x/c = 0.3, 0.4$ and 0.5). From left to right are $x/c = 0.15, 0.2, 0.3, 0.4$ and 0.5 , respectively. Displayed are envelopes for two extreme Δ_k perturbations considered in this study: $\Delta_k = 0.1$ (red envelope), $\Delta_k = 8$ (gray envelope), and M_k (blue envelope). The baseline prediction is provided for reference. \circ in-house DNS data³⁴.

3. Reynolds shear stress

The predicted profiles for the Reynolds shear stress normalized with the freestream velocity squared, $-\langle u_1 u_2 \rangle / U_\infty^2$ are shown in Fig. 18. Undergoing the $\Delta_k = 0.1$ and $\Delta_k = 8$ perturbations, an enveloping behavior with respect to the baseline prediction can be observed. Figure 18 shows that the baseline prediction for the $-\langle u_1 u_2 \rangle / U_\infty^2$ profile at $x/c = 0.15$ significantly over-predicts the in-house DNS profile, implying a higher level of momentum transfer due to the Reynolds shear stress. In the aft portion of the LSB and downstream of the LSB near the reattachemnt point (X_R), the predictions for the $-\langle u_1 u_2 \rangle / U_\infty^2$ profiles at $x/c = 0.2$ and $x/c = 0.3$ exhibit a shape of parabolic arch, revealing a same effect as the in-house DNS data, i.e., a strong increase in the Reynolds shear stress profile around the peak of the parabolic arch. The magnitude of the increase is much greater for the in-house DNS data probably due to the larger height of the LSB produced than the baseline prediction. Further downstream of the LSB, the baseline predictions for the $-\langle u_1 u_2 \rangle / U_\infty^2$ profiles at $x/c = 0.4$ and $x/c = 0.5$ (in the attached turbulent boundary layer) show relatively good agreement with the in-house DNS data, although some discrepancies exist in the regions next to the wall and in the upper section of the Reynolds shear stress profiles.

In Fig. 18, the $\Delta_k = 0.1$ perturbation increases the magnitude of the $-\langle u_1 u_2 \rangle / U_\infty^2$ profile compared to the baseline prediction. In the aft portion of the LSB ($x/c = 0.15, x/c = 0.2$ and $x/c = 0.3$), the $\Delta_k = 0.1$ perturbations retain the shape of parabolic arch, with a peak value around the maximum height of the arch gradually reducing in magnitude to zero from the peak in the opposite directions toward the wall and the OBL, respectively. In addition, the $\Delta_k = 0.1$ perturbations increase the momentum transfer due to the Reynolds shear stress compared to the baseline prediction. Consequently, the $\Delta_k = 0.1$ perturbations tend to approach closer to the in-house DNS data except at $x/c = 0.15$, where a deviation from the in-house DNS data is observed. As the flow proceeds fur-

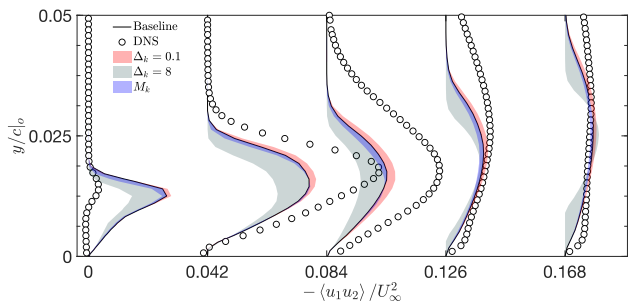


FIG. 18. Reynolds shear stress profiles in the aft portion of the LSB ($x/c = 0.15$ and 0.2) and in the attached TBL ($x/c = 0.3, 0.4$ and 0.5). From left to right are $x/c = 0.15, 0.2, 0.3, 0.4$ and 0.5 , respectively. Displayed are envelopes for two extreme Δ_k perturbations considered in this study: $\Delta_k = 0.1$ (red envelope), $\Delta_k = 8$ (gray envelope), and M_k (blue envelope). The baseline prediction is provided for reference. \circ in-house DNS data³⁴.

ther downstream within the attached turbulent boundary layer ($x/c = 0.4$ and $x/c = 0.5$), the effect of the $\Delta_k = 0.1$ perturbation gradually deteriorates with x/c , with some of the in-house DNS data being encompassed.

On the other hand, the $\Delta_k = 8$ perturbation decreases the magnitude of the $-\langle u_1 u_2 \rangle / U_\infty^2$ profile compared to the baseline prediction, with the size of the uncertainty bound significantly larger than that for the $\Delta_k = 0.1$ perturbation, reflecting the simulation’s much stronger response to the $\Delta_k = 8$ perturbation. Likewise, a shape of parabolic arch and a similar behavior to the $\Delta_k = 0.1$ perturbations are observed for the $\Delta_k = 8$ perturbations in the aft portion of the LSB ($x/c = 0.15$, $x/c = 0.2$ and $x/c = 0.3$) as well: peaking around the maximum height of the parabolic arch and gradually decreasing in magnitude toward the wall and OBL. As a result, the $\Delta_k = 8$ perturbations reduce the momentum transfer due to the Reynolds shear stress to a great extent around the peak of the parabolic arch. This shows a tendency for the $\Delta_k = 8$ perturbations to deviate from the in-house DNS data except at $x/c = 0.15$, where the $\Delta_k = 8$ perturbations tend to approach closer to the in-house DNS profile that much lag behind the baseline prediction. Within the attached turbulent boundary layer ($x/c = 0.4$ and $x/c = 0.5$), an important observation for the $\Delta_k = 8$ perturbation is that the uncertainty bounds retain a value of zero not only at the wall but also extend for some distance above the wall, which violates the “rule” that all Reynolds stresses decrease to zero at the wall surface due to the no-slip wall condition⁶¹. This marks the behavior of “over perturbation” with $\Delta_k = 8$, and is not physically realizable. Since few studies have been conducted to determine the upper bound of k^* , this study here sheds light on a possible way of determining the upper bound of k^* using the result of Reynolds shear stress. Therefore, the maximum magnitude of Δ_k must ensure that Reynolds stresses must behave in a physically-realizable manner in the near-wall region.

The M_k perturbation in general under-predicts the baseline prediction across the suction side, in general sitting within the gray envelope, with a subtle movement to the red envelope being discerned in the lower section of the Reynolds shear stress

profiles for $x/c = 0.2$ and $x/c = 0.3$. Within the attached turbulent boundary layer ($x/c = 0.4$ and $x/c = 0.5$), the uncertainty bounds generated from the M_k perturbation remain constantly below the baseline prediction, which is consistent with the uniform magnitude of $\Delta_k = 2.8$. It should be noted that the simulation’s response to the perturbed Reynolds shear stress profile is in general stronger than that for the perturbed mean velocity profile. This indicates that the level of sensitivity to the Δ_k perturbation varies with different QoIs being observed. In Fig. 18, the M_k function successfully avoids over-perturbations through strictly comparing to the available high-fidelity data, ensuring that only the physical realistic perturbations are considered.

C. Combining M_k with $1c$, $2c$, and $3c$

1. Skin friction coefficient

Distributions of the skin friction coefficient and the pressure coefficient, C_f and C_p , are shown in Figs. 19 (a) and (b), respectively. Also included are the in-house DNS³⁴ and ILES/LES data of⁵⁰ and⁴⁹ for comparison. Integrating the M_k perturbation with the eigenvalue perturbation ($1c$, $2c$ and $3c$) using Eqs. 8, 23 and 24 yields compound effect, namely, $1c_M_k$, $2c_M_k$ and $3c_M_k$. Also included are the eigenvalue perturbation ($1c$ and $3c$) as a reference for the $1c_M_k$, $2c_M_k$ and $3c_M_k$ perturbation. In the aft portion of the LSB, Fig. 19 (a) clearly shows that the $1c_M_k$ perturbation decreases the magnitude of C_f more than the $2c_M_k$ perturbation does compared to the baseline prediction, while the $3c_M_k$ perturbation results in the uncertainty bound that almost overlaps the one generated from the $3c$ perturbation, indicating simulation’s low sensitivity to the $3c_M_k$ perturbation. In addition, both uncertainty bounds generated from the $3c_M_k$ and $3c$ perturbations in general sit slightly below the baseline prediction except at the trough around $x/c = 0.2$ (in the aft portion of the LSB), where they sit somewhat above the baseline prediction. As a consequence, an enveloping behavior with respect to the baseline prediction is observed. On the other hand, the uncertainty bounds generated from the $1c_M_k$ and $2c_M_k$ perturbations lie significantly above the baseline prediction, encompassing the reference data for X_R , as well as the steep rise followed by X_R . Interestingly, it is clear that this promising increase associated with the $1c_M_k$ and $2c_M_k$ perturbations is not a simple sum of the M_k and $1c/2c$ uncertainty bounds up, but a “synergy” has developed. Moreover, the synergy behavior associated with the $1c_M_k$ perturbation results in the encompassing of the gap between the baseline prediction and the reference data in the aft portion of the LSB as well as at the crest. Besides, it is interesting to note that the uncertainty bounds generated from $1c_M_k$ and $2c_M_k$ perturbations tend to retain the shape of the C_f profile at the crest for $0.3 < x/c < 0.4$, with the $1c_M_k$ perturbation effectively encompassing the in-house DNS data of³⁴. This confirms the effect of spatial variability in M_k . As the flow proceeds further downstream $0.4 < x/c < 0.6$, a rapid collapse of the uncertainty bounds generated from the $1c_M_k$ and $2c_M_k$ perturba-

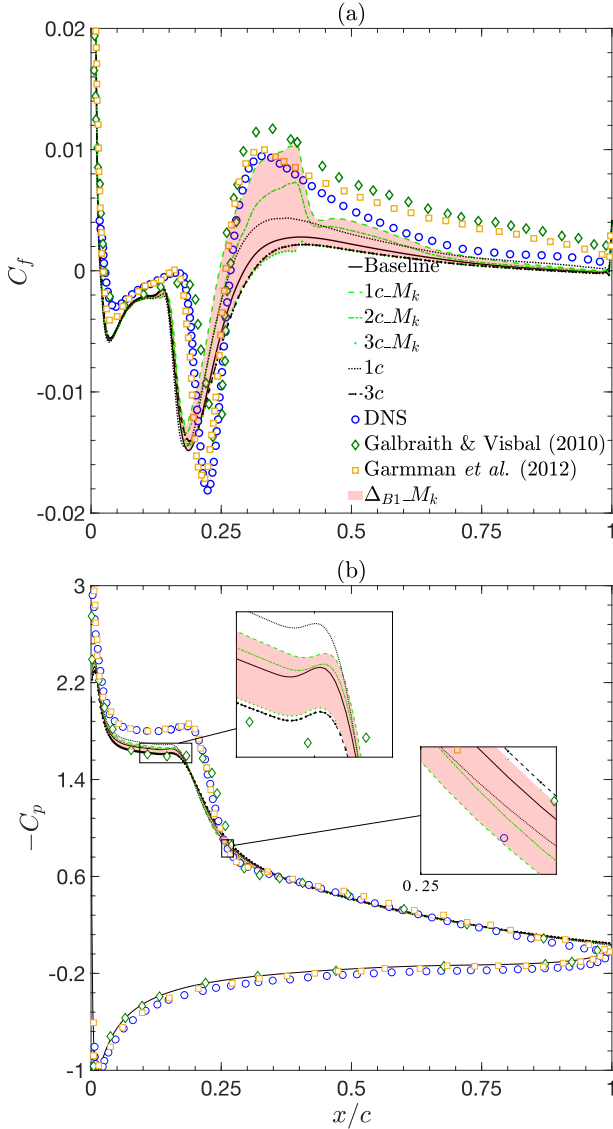


FIG. 19. (a) Profile of skin friction coefficient and (b) pressure coefficient with enlarged regions at the flat spot and the kink followed by a sharp drop of C_p . Displayed are uncertainty bounds for $1c_{M_k}$, $2c_{M_k}$ and $3c_{M_k}$ perturbations (red envelope). Δ_{B1} stands for $\Delta_B = 1.0$. Profiles of baseline prediction and eigenvalue perturbations ($1c$ and $3c$) are provided for reference. \circ in-house DNS data³⁴.

tions is observed. This confirms the uniform magnitude of M_k used in the region for $0.4 < x/c < 0.6$. On the other hand, the $3c_{M_k}$ and $3c$ perturbations become almost indistinguishable from each other, lying somewhat below the baseline prediction across the entire suction side, except for a slight decrease found associated with the $3c_{M_k}$ perturbation in the region for $0.35 < x/c < 0.4$.

In Fig. 19 (b), at the flat spot the $1c_{M_k}$ perturbation increases the magnitude of C_p more than the $2c_{M_k}$ perturbation does compared to the baseline prediction. Both $1c_{M_k}$ and $2c_{M_k}$ perturbations show a tendency to approach toward the in-house DNS³⁴ and LES data of⁴⁹, and sit within the

uncertainty bound generated from the $1c$ perturbation. Interestingly, there is no discernible synergy behavior appearing at the flat spot, the uncertainty bound generated from the $1c_{M_k}$ and $2c_{M_k}$ perturbations tend to reduce somewhat in size compared to the $1c$ and $2c$ perturbations instead. On the other hand, the uncertainty bounds generated from the $3c_{M_k}$ and $3c$ perturbations become almost indistinguishable at the flat spot, sitting slightly below the baseline prediction in a trend of approaching toward the ILES data of⁵⁰. At the kink around X_R , the uncertainty bounds generated from the $1c_{M_k}$ and $2c_{M_k}$ perturbations under-predict the baseline prediction and tend to approach closer to the reference data, while the uncertainty bound for the $3c_{M_k}$ perturbation over-predicts the baseline prediction and retains the behavior of collapsing onto the $3c$ perturbation, showing a trend of deviating from the reference data. As a consequence, a discernible enveloping behavior with respect to the baseline prediction is observed at both the flat spot and the kink around X_R , where most uncertainty is generated, as shown in Fig. 19 (b). In addition, the collapsing behavior of the $3c_{M_k}$ and $3c$ perturbations at the flat spot and the kink indicates the simulation's low sensitivity to the $3c_{M_k}$ perturbation. Compared to C_f , it is clear that C_p overall is less sensitive to all kinds of perturbations. This is because the wall pressure is determined by the freestream, which is only modified minutely by the eigenvalue perturbations⁹. In addition, this reflects that the degree of response to the Δ_k perturbation varies with which QoIs being observed. On the pressure side, the simulation's response to all kinds of perturbations are rather small, indicating a low level of model form uncertainty and hence high trustworthiness in the baseline prediction for C_p .

It should be noted that because $3c$ perturbation retains the isotropic nature of the turbulent viscosity model, it yields limited influence on the perturbed results³¹. This is well reflected in the smaller size of the uncertainty bound generated from the $3c$ perturbation compared to the $1c$ and $2c$ perturbations. Such inefficacy of $3c$ perturbation has been observed by Emory *et al.*⁹ as well. Importantly, this inefficacy persists when being compounded with M_k , which might partly explain the collapsing behavior of the $3c_{M_k}$ profile onto the $3c$ profile as can be observed in Figs. 19 (a) and (b). Moreover, this collapsing behavior not only happens to the results of C_f and C_p but also happens to the mean velocity profile and the turbulence quantities, as can be observed in the following sections.

2. Mean velocity field

Contours of the mean velocity normalized by the freestream velocity, $\langle U \rangle / U_\infty$ from the baseline, $1c_{M_k}$, $2c_{M_k}$ and $3c_{M_k}$ perturbations, eigenvalue perturbations ($1c$, $2c$ and $3c$), M_k perturbation and in-house DNS of³⁴ in an xy plane are shown in Fig. 20. From Fig. 20, all of the $\langle U \rangle / U_\infty$ contours show a recirculating region, i.e., the eye-like green region, where the negative value of velocity is present. In addition, the mean velocity contour generated from the M_k perturbation results in a shorter LSB and a slightly increased $\langle U \rangle / U_\infty$ in magnitude in the region downstream of the reattachment

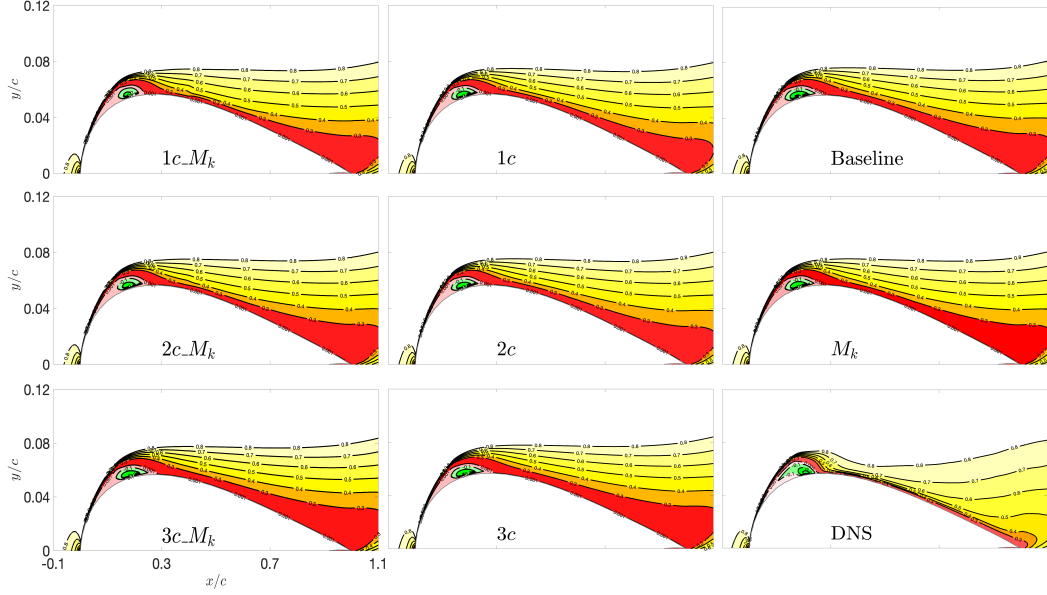


FIG. 20. Contours of $\langle U \rangle / U_\infty$ with $1c_M_k$, $2c_M_k$, $3c_M_k$, $1c$, $2c$, $3c$ and M_k perturbations in an xy plane. Isolines of the mean streamwise velocity are superimposed on the contour plots. The contour of baseline prediction is provided for reference, and the contour of in-house DNS data³⁴ is included for comparison.

point $0.3 < x/c < 0.6$, in which the untrustworthy zones are identified. This indicates that the M_k perturbation tends to suppress the LSB compared to the baseline prediction. This reduces the turbulence kinetic energy contained in the large-scale coherent structures⁶⁰, implying the increased mean-flow energy in the vicinity of the LSB $0.3 < x/c < 0.6$, therefore increased magnitude of $\langle U \rangle / U_\infty$ in this region, as shown in Fig. 20. For the $1c$ and $2c$ eigenvalue perturbations, the contours show a reduction in the length of the LSB compared to the baseline prediction, which results in an overall increase in the mean-flow magnitude further downstream of the reattachment point, while the $3c$ perturbation does the opposite. In addition, it is clear that the $1c_M_k$ and $2c_M_k$ perturbations further increase the magnitude of $\langle U \rangle / U_\infty$ than the $1c$ and $2c$ perturbations do compared to the baseline prediction, which confirms the greatly reduced C_f in magnitude in the aft portion of the LSB, while the $3c_M_k$ perturbation remains at nearly same magnitude as that for the $3c$ perturbation, which confirms the collapse of the C_f profiles generated from the $3c_M_k$ and $3c$ perturbations, as shown in Fig. 19 (a). This indicates a weak compound effect of the $3c_M_k$ perturbation. Compared to the baseline prediction, both $1c_M_k$ and $2c_M_k$ perturbations shorten the region of reverse flow (deviating from the in-house DNS data), while increase the mean-flow magnitude in the attached turbulent boundary layer (approaching closer to the in-house DNS data); on the other hand, the $3c_M_k$ perturbation bolsters the region of reverse flow, showing a tendency of approaching closer to the in-house DNS data, while shows a reduction in the magnitude of $\langle U \rangle / U_\infty$ in the attached turbulent boundary layer, causing a deviation from the in-house DNS data.

The predictions for the mean velocity profile normalized

by U_∞ , i.e., $\langle U \rangle / U_\infty$, are presented in Figs. 21 (a) - (e). The in-house DNS data of³⁴ is included for comparison. In Figs. 21 (a) - (e), the $1c$ and $3c$ eigenvalue perturbations are used as a reference for the $1c_M_k$, $2c_M_k$ and $3c_M_k$ perturbation. From Figs. 21 (a) - (e), an enveloping behavior with respect to the baseline prediction is observed, i.e., the $1c_M_k$ and $2c_M_k$ perturbations leading the baseline prediction, while the $3c_M_k$ perturbation lagging behind. A similar behavior of the $1c$ and $3c$ perturbations with respect to the baseline prediction was also observed by Luis *et al.*¹⁴ in their numerical study for a turbulent flow over a backward-facing step. In addition, the $3c_M_k$ profile tends to collapse onto the $3c$ profile, reflecting the simulation's low sensitivity to the $3c_M_k$ perturbation, which is consistent with the behavior shown in Fig. 20. At $x/c = 0.15$ (X_T), the uncertainty bound generated from the $1c_M_k$ perturbation increases the magnitude of the mean velocity profile more than the $2c_M_k$ perturbation does in both the region of reverse flow ($U/U_\infty < 0$) for $0 < y/c|_o < 0.007$ and the upper portion of the boundary layer for $0.011 < y/c|_o < 0.023$, showing a tendency to approach closer to the in-house DNS data. On the other hand, the $3c_M_k$, $3c$ and baseline profiles show a collapse, indicating a type of similarity. This might be partly explained by the almost same values of C_f found in the $3c_M_k$, $3c$ and baseline profiles around X_T , as shown in Fig. 19 (a). It should be noted that the uncertainty bounds generated from the $1c_M_k$, $2c_M_k$, and $3c_M_k$ perturbations and the baseline prediction are negligibly small for $0.007 < y/c|_o < 0.011$, i.e., all collapsing onto a single curve, which shows good agreement with the in-house DNS data, as shown in Fig. 21 (a). This reveals a low level of the model form uncertainty and hence relatively high trustworthiness in this region. As the flow moves fur-

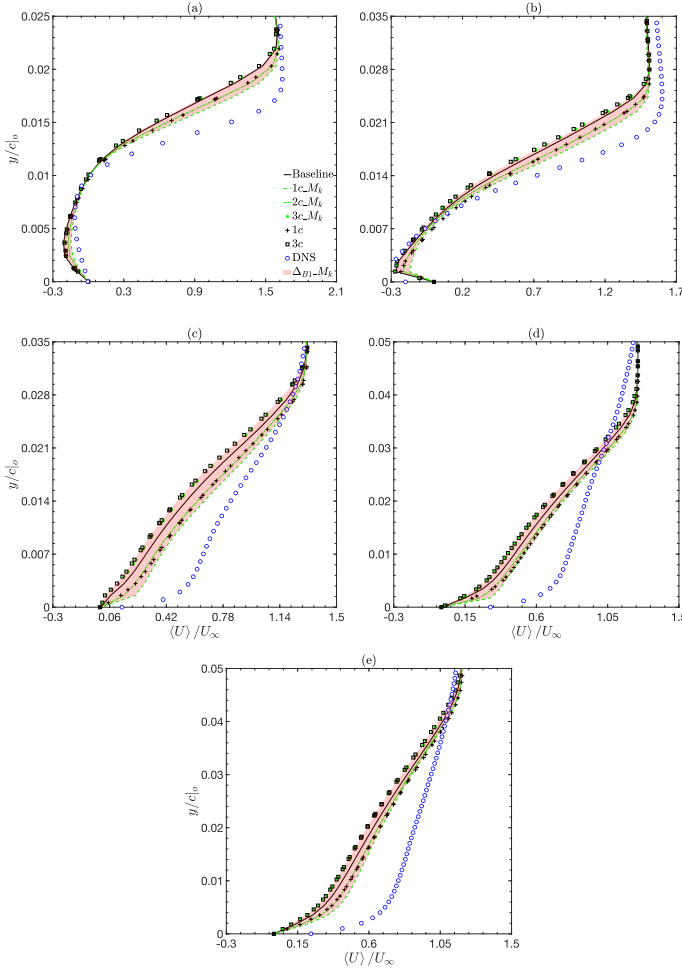


FIG. 21. Profile of $\langle U \rangle / U_\infty$ in the aft portion of the LSB for (a) $x/c = 0.15$ and (b) $x/c = 0.2$; and profile of $\langle U \rangle / U_\infty$ in the attached TBL for (c) $x/c = 0.3$, (d) $x/c = 0.4$ and (e) $x/c = 0.5$. Displayed are uncertainty bounds for $1c_M_k$, $2c_M_k$ and $3c_M_k$ perturbations (red envelope). Δ_{B1} stands for $\Delta_B = 1.0$. Profiles of baseline prediction and eigenvalue perturbations ($1c$ and $3c$) are provided for reference. \circ in-house DNS data³⁴.

ther downstream to $x/c = 0.2$ (the aft portion of the LSB), the effect of the $1c_M_k$ and $2c_M_k$ perturbations has permeated the entire boundary layer, showing a tendency of approaching closer to the in-house DNS data in the upper portion of the boundary layer. Moreover, the uncertainty bounds generated from the $1c_M_k$ and $2c_M_k$ perturbations over-predict the baseline prediction but lie somewhat above the $1c$ perturbation in the region for $0.007 < y/c|_o < 0.011$, overall showing closer agreement with the in-house DNS data, as shown in Fig. 21 (b). Again, this reflects the effect of spatial variability in M_k . Note that the baseline prediction overall shows good agreement with the in-house DNS data in the region of reverse flow at $x/c = 0.2$, at which the baseline prediction, $3c$, and $3c_M_k$ perturbations collapse onto a single curve. The almost identical magnitude of C_f retained by the $3c_M_k$, $3c$ and baseline predictions for $x/c = 0.2$, as shown in Fig. 19 (a), might partly explain this type of similarity. Away from the

wall, a collapsing behavior is again observed for the $3c_M_k$ and $3c$ perturbations, with a slight offset from the baseline prediction. Note that the $1c$ perturbation is well encompassed by $1c_M_k$ in the aft portion of the LSB, as shown in Figs. 21 (a) - (b). This confirms the larger values of C_f for the $1c_M_k$ perturbation in this region. At $x/c = 0.3$ (downstream of the LSB near X_R), $x/c = 0.4$ and $x/c = 0.5$ (in the reattached turbulent boundary layer), the uncertainty bounds generated from the $1c_M_k$ and $2c_M_k$ perturbations in general tend to approach closer to the in-house DNS data, with the perturbation effect gradually deteriorating further downstream. This is consistent with the gradual reduction in the positive values of C_f as the flow moves further downstream of X_R , as shown in Fig. 19 (a). Also the difference between the $1c$ and $1c_M_k$ perturbation becomes smaller, which confirms the comparable magnitude of C_f in the region of the attached turbulent boundary layer, as shown in Fig. 19 (a). On the other hand, a collapse is also observed for the $3c_M_k$ and $3c$ perturbations at $x/c = 0.4$ and $x/c = 0.5$, which confirms the almost identical values of C_f retained by the $3c_M_k$ and $3c$ perturbations shown in Fig. 19 (a). It is interesting to note that $1c$ and $2c$ perturbations respond favorably to M_k , while $3c$ perturbation remains almost immune to it.

Figure 22 shows contours of mean velocity, with the region of reverse flow being enlarged. The region of reverse flow is evidenced by the velocity vectors added in the LSB. The baseline prediction is provided for reference. Also included is the in-house DNS data of³⁴ for comparison. Compared to the in-house DNS data, Fig. 22 clearly shows that the baseline prediction shifts the region of reverse flow in the upstream direction. Within the LSB (green region), the velocity vectors for the $1c$ and $2c$ perturbations clearly indicate a subdued reverse-flow field, resulting in a shorter LSB and hence a better agreement with the DNS data, and the opposite is true for the $3c$ perturbation. For the attached turbulent boundary layer, the velocity vectors indicate an overall increase in the mean velocity field for the $1c$ and $2c$ perturbations, showing a tendency of approaching to the DNS mean flow field, while the $3c$ perturbation shows an overall reduction in the mean velocity field. Integrating M_k into the $1c$, $2c$, and $3c$ perturbation tends to suppress the size of the LSB, but increases the mean flow field downstream of the LSB. Among these perturbations, $1c_M_k$ increases the mean flow field more than $2c_M_k$ in the attached turbulent boundary layer, to the largest extent contributing to a closer approach to the in-house DNS data.

3. Reynolds shear stress

Contours of the Reynolds shear stress normalized by the freestream velocity squared, $-\langle u_1 u_2 \rangle / U_\infty^2$ from the baseline, $1c_M_k$, $2c_M_k$ and $3c_M_k$ perturbations, eigenvalue perturbations ($1c$, $2c$, $3c$), M_k perturbation in an xy plane are shown in Fig. 23. Also included is the in-house DNS data of³⁴ for comparison. In Fig. 23, all of the $-\langle u_1 u_2 \rangle / U_\infty^2$ contour plots show a peak around X_T , i.e., the bright yellow region, downstream from the peak a gradual reduction in the magnitude of $-\langle u_1 u_2 \rangle / U_\infty^2$ is observed. From Fig. 23, the M_k pertur-

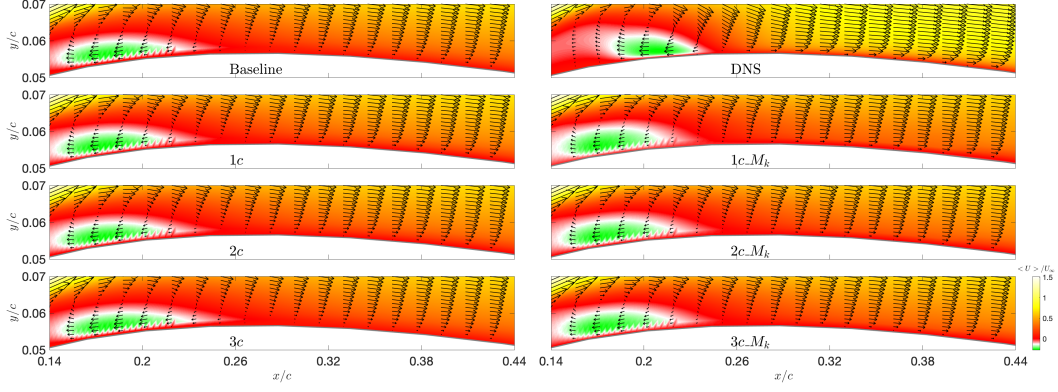


FIG. 22. Contours of normalized mean velocity $\langle U \rangle / U_\infty$ with in-plane velocity vectors superimposed on the contours in an xy plane. The region in the vicinity of the wall is enlarged to highlight the flow behavior in the LSB, as well as in the turbulent region right downstream of the LSB. A focus on a section of the airfoil suction side is considered: $0.14 < x/c < 0.44$.

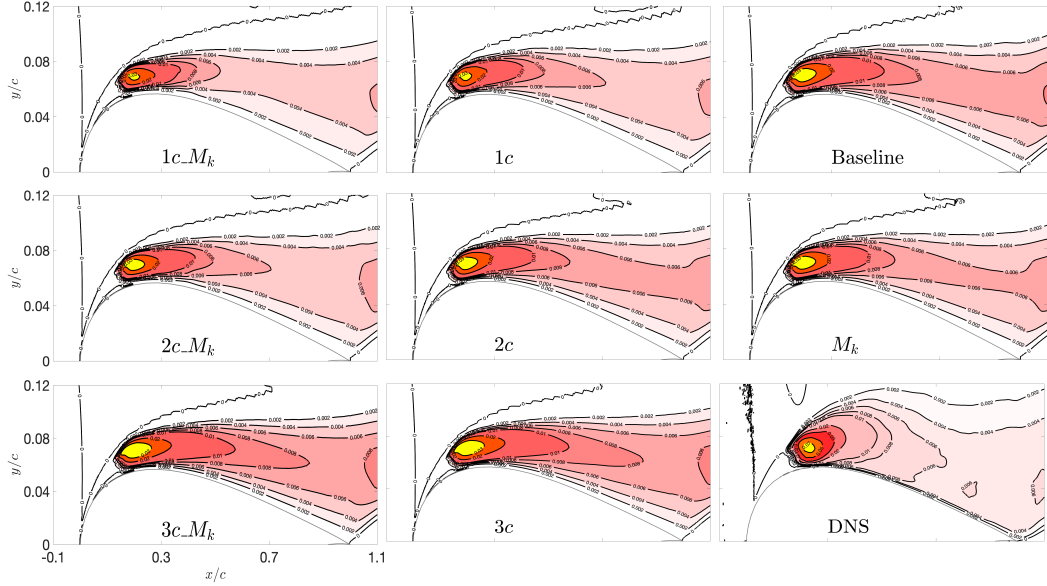


FIG. 23. Contours of $-\langle u_1 u_2 \rangle / U_\infty^2$ with $1c_Mk$, $2c_Mk$, $3c_Mk$, $1c$, $2c$, $3c$ and M_k perturbations in an xy plane. Isolines of the Reynolds shear stress are superimposed on the contour plots. The contour of baseline prediction is provided for reference, and the contour of in-house DNS data³⁴ is included for comparison.

bation overall reduces the magnitude of $-\langle u_1 u_2 \rangle / U_\infty^2$ in both the transitional and turbulent region compared to the baseline prediction. From Fig. 23, it is clear that the $1c_Mk$ and $2c_Mk$ perturbations further reduce the magnitude of $-\langle u_1 u_2 \rangle / U_\infty^2$ compared to the $1c$ and $2c$ perturbations, while the $3c_Mk$ perturbation remains at a nearly same magnitude as that of the $3c$ perturbation. In addition, the $1c_Mk$ and $2c_Mk$ perturbations under-predict the baseline prediction, and in general tend to approach closer to the in-house DNS data in the attached turbulent boundary layer, although an under-prediction for $-\langle u_1 u_2 \rangle / U_\infty^2$ is observed in the LSB; on the other hand, the $3c_Mk$ perturbation over-predicts the baseline prediction, showing better agreement with the in-house DNS data within the LSB.

The predicted profiles for the Reynolds shear stress normalized by the freestream velocity squared, $-\langle u_1 u_2 \rangle / U_\infty^2$, are shown in Figs. 24 (a) - (e). Also included are the in-house DNS data of³⁴ for comparison, as well as the $1c$ and $3c$ eigenvalue perturbations used as a reference for the $1c_Mk$, $2c_Mk$ and $3c_Mk$ perturbations. Figures 24 (a) - (e) show that the baseline prediction is well enveloped by the uncertainty bounds generated from the $1c_Mk$, $2c_Mk$ and $3c_Mk$ perturbations. In addition, the $1c_Mk$ and $2c_Mk$ perturbations reduce the magnitude of the predicted $-\langle u_1 u_2 \rangle / U_\infty^2$ profiles compared to the baseline prediction, while the $3c_Mk$ perturbation does the opposite. A similar behavior of the $1c$ and $3c$ perturbations with respect to the baseline prediction was also observed by Luis *et al.*¹⁴ in their numerical study for a

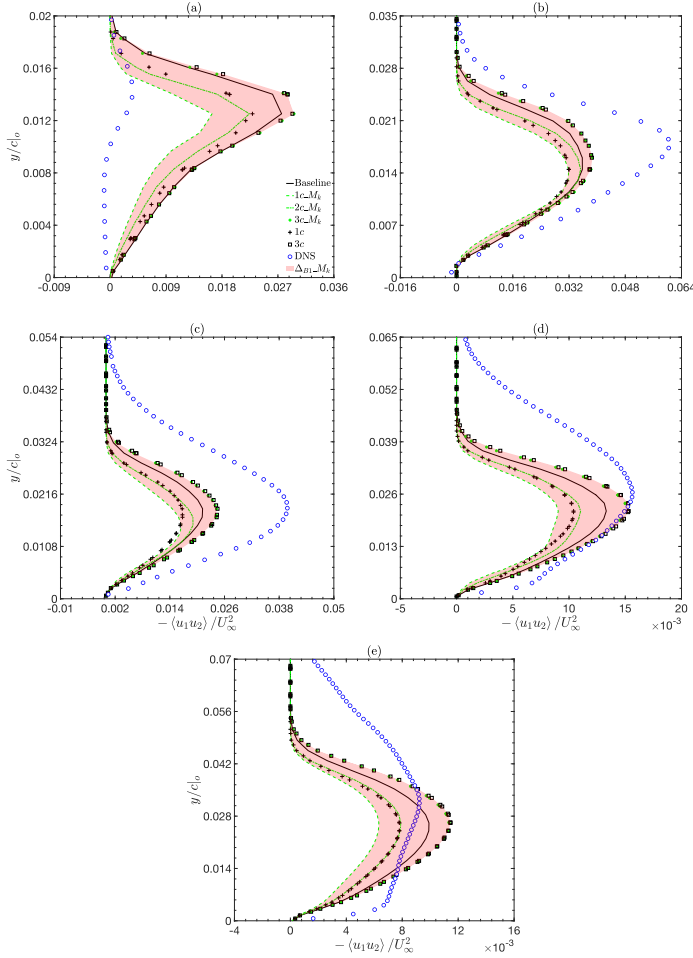


FIG. 24. Profile of $-\langle u_1 u_2 \rangle / U_\infty^2$ in the aft portion of the LSB for (a) $x/c = 0.15$ and (b) $x/c = 0.2$; and profile of $-\langle u_1 u_2 \rangle / U_\infty^2$ in the attached TBL for (c) $x/c = 0.3$, (d) $x/c = 0.4$ and (e) $x/c = 0.5$. Displayed are uncertainty bounds for $1c_M_k$, $2c_M_k$ and $3c_M_k$ perturbations (red envelope). Δ_{B1} stands for $\Delta_B = 1.0$. Profiles of baseline prediction and eigenvalue perturbations ($1c$ and $3c$) are provided for reference. \circ in-house DNS data³⁴.

turbulent flow over a backward-facing step. Figures 24 (a) - (e) show that the simulation’s sensitivity to the $3c_M_k$ perturbation is rather low, with the $3c_M_k$ profile nearly collapsing onto the $3c$ profile. A similar behavior is also observed in Fig. 21 (a) - (e). At $x/c = 0.15$ (X_T), Fig. 24 (a) shows that the $1c_M_k$ perturbation results in a rather strong reduction in the magnitude of $-\langle u_1 u_2 \rangle / U_\infty^2$ across the entire boundary layer compared to the baseline prediction, showing a tendency of approaching closer to the in-house DNS data, and a “synergy behavior” is observed. On the other hand, the $3c_M_k$ perturbation that tends to deviate from the in-house DNS data, indicating a weak response to the M_k perturbation. In Figs. 24 (b) - (e), the baseline predictions and in-house DNS data are similar in shape: the convexity of the profile strongly increases in the vicinity of the wall, and then relaxes as the distance from the wall increases, with some discrepancies that overall mark the under-prediction of the momentum transfer

due to the Reynolds shear stress within both the transitional and turbulent boundary layer. Therefore, there is an important observation: the synergy behavior seems only active for the $1c_M_k$ and $2c_M_k$ perturbations. As the flow moves further downstream to $x/c = 0.2$ (the aft portion of the LSB) and $x/c = 0.3$ (downstream of the LSB near X_R), the $1c_M_k$ perturbation decreases the predicted Reynolds shear stress more than the $1c$ perturbation does in the outer portion of the boundary layer, indicating a deviation from the in-house DNS data, while shows a somewhat reduction and no discernible change (a collapse onto the $1c$ profile) at $x/c = 0.2$ and $x/c = 0.3$, respectively, in the near-wall region, as shown in Figs. 24 (b) and (c). This reflects the spatial variability in M_k . On the other hand, the $-\langle u_1 u_2 \rangle / U_\infty^2$ profiles generated from the $3c_M_k$ perturbations nearly collapse onto that for the $3c$ perturbations at $x/c = 0.2$ and $x/c = 0.3$; consequently, the $-\langle u_1 u_2 \rangle / U_\infty^2$ profiles generated from the $3c_M_k$ perturbations tend to approach closer to the in-house DNS data at $x/c = 0.2$ and $x/c = 0.3$, as shown in Figs. 24 (b) and (c). At $x/c = 0.4$ and $x/c = 0.5$ (in the attached turbulent boundary layer), a synergy behavior is again observed for the $1c_M_k$ perturbations across the entire boundary layer, which enhances the deviation from the in-house DNS data at $x/c = 0.4$, while encompasses the in-house DNS data at $x/c = 0.5$. On the other hand, a collapse is again observed for the $3c_M_k$ and $3c$ perturbations. Besides, the uncertainty bounds generated from the $2c_M_k$ and $3c_M_k$ perturbations successfully encompass the in-house DNS data in the lower portion of the attached turbulent boundary layer at $x/c = 0.4$ and $x/c = 0.5$, although there is a small discrepancy present in the region next to the wall.

VI. CONCLUSIONS

The goal of the present study was to advance our understanding of a physics-based methodology to quantify transition model-form uncertainty in RANS predictions of unsteady flow over a SD7003 airfoil. The method is based on the framework proposed in the study of⁹, which introduces perturbations to a decomposition of the Reynolds stress tensor, namely, the amplitude and the eigenvalue of the anisotropy Reynolds stress tensor. In this study, the methodology was completely implemented in C++ in OpenFOAM. Based on the baseline predictions for C_f and C_p , we presented analyses to locate the untrustworthy region, which is further divided into four zones to cover both the LSB and turbulent flow region further downstream. A novel regression based marker function was developed to inject an accurate level of the amplitude perturbation into the identified untrustworthy region.

We presented analyses to understand the effect of the uniform amplitude perturbation to the skin friction coefficient, mean velocity, and Reynolds shear stress. Importantly, we observed a monotonic behavior of the magnitude of the predicted bounds with Δ_k perturbations, in particular more noticeable bounds for $\Delta_k > 1$: a clear shift of the reattachment point in the upstream direction, a noticeable suppression of the length of the LSB, and a greatly reduced magnitude of Reynolds shear stress in the LSB region; for the turbulent flow region further

downstream of the LSB, results for both the mean velocity and the Reynolds shear stress showed better agreement with the in-house DNS data of³⁴. Such monotonic behavior is imperative for the development of a marker function that aims to predict plausible bounds for QoIs.

The predicted bounds generated from the marker function M_k was contrasted with the uniform amplitude perturbations $\Delta_k = 0.1$ and $\Delta_k = 8$ for different QoIs. Results for the QoIs clearly showed the spatial variability in M_k , and the bounds generated from M_k in general sat within the bounds generated from $\Delta_k = 8$. The $\Delta_k = 8$ perturbations showed a clear tendency to approach closer to the reference data^{34,49,50} for C_f and C_p , and well encompassed the reattachment point in the predicted bounds. Overall, the $\Delta_k = 0.1$ perturbation was the opposite of the behavior of $\Delta_k = 8$: deviating from the reference data and showing rather small bounds. On the pressure side, the C_p profile for $\Delta_k = 0.1$, baseline prediction, and $\Delta_k = 8$ showed a collapse, which indicated a low model form uncertainty. Importantly, the over-perturbation behavior associated with the predicted Reynolds shear stress profile undergoing the $\Delta_k = 8$ perturbation could facilitate the approximating of the upper-bound of the amplitude perturbation.

When compounding M_k with the eigenvalue perturbations $1c$, $2c$, the predicted bounds for C_f was dramatically increased to encompass the reattachment point and the reference data of^{34,49,50} at the crest, which showed a synergy behavior and consistently sat above the baseline prediction. Overall, the uncertainty bounds retained the shape of the baseline prediction for C_f , which confirmed the effect of spatial variability in M_k . The predicted $1c_M_k$ and $2c_M_k$ bounds for C_p sat above the baseline prediction at the flat spot, which did not exhibit a synergy behavior, but reduced in magnitude compared to the $1c$ and $2c$ perturbations instead. The opposite was true at the kink (or the reattachment point) of the C_p distribution, where the $1c_M_k$ and $2c_M_k$ perturbations under-predicted the baseline prediction. The $3c$ and $3c_M_k$ bounds for both C_f and C_p showed a collapse, which deviated slightly away from the baseline prediction. the perturbed mean velocity profile approached a lot closer to the in-house DNS data near the reattachment point.

When the contours of the mean velocity were plotted in an xy plane, the $1c$ and $2c$ perturbations suppressed the LSB compared to the baseline prediction, which increased the magnitude of the mean flow. This behavior was enhanced by compounding with M_k : $1c_M_k$ and $2c_M_k$ further increased the magnitude of the mean flow in the attached turbulent boundary layer through a more suppression of the LSB. This behavior is qualitatively similar to that observed in the in-house DNS contour³⁴. Again, the $3c_M_k$ remained at nearly same magnitude as that for the $3c$ perturbation, which bolstered the region of reverse flow to approach closer to the in-house DNS data³⁴. When the predictions for the mean velocity profile were plotted in coordinates shifted vertically, the predicted bounds generated from the $1c_M_k$ and $2c_M_k$ perturbations in general led ahead the baseline prediction, while the $3c_M_k$ perturbation lagged behind it, which showed an enveloping behavior with respect to the baseline prediction. This behavior is qualitatively similar to the $1c$ and $3c$ perturbations observed

by Luis *et al.*¹⁴. At the transition point X_T , all of the perturbations and the baseline prediction showed a collapse for $0.007 < y/c|_o < 0.011$, and showed a good agreement with the in-house DNS data³⁴. As the flow moves further downstream of X_R , the $1c_M_k$ and $2c_M_k$ perturbations showed a tendency to approach closer to the in-house DNS data, while the effect of perturbation gradually deteriorated due to gradual reduction in the positive values of C_f . Overall, the compound effect of $3c_M_k$ was weak, which indicated the immunity of the $3c$ perturbation to the marker function. With the velocity vectors added to the mean velocity contour, a clear visualization again, confirmed the effect of all of the perturbations in the region of reverse flow and the attached turbulent boundary layer.

The dimensionless Reynolds shear stress contours in an xy plane were also analyzed. The $1c_M_k$ and $2c_M_k$ perturbations under-predicted the baseline prediction, which showed a tendency to approach closer to the in-house DNS data in the region downstream of the LSB. While, the $3c_M_k$ perturbation over-predicted the baseline prediction, and showed good agreement with the in-house DNS data³⁴ in the region of the LSB. When the predictions for the dimensionless Reynolds shear stress $-\langle u_1 u_2 \rangle / U_\infty^2$ profile were plotted, the $1c_M_k$ and $2c_M_k$ perturbations reduced the magnitude of the $-\langle u_1 u_2 \rangle / U_\infty^2$ profiles compared to the baseline prediction, while the $3c_M_k$ perturbation did the opposite, which resulted in an enveloping behavior. This behavior is qualitatively similar to that observed by Luis *et al.* At the transition point, the $1c_M_k$ perturbation greatly reduced the magnitude of the $-\langle u_1 u_2 \rangle / U_\infty^2$ profile, which marked a synergy behavior. An important observation was that the synergy behavior seems only active for the $1c_M_k$ and $2c_M_k$ perturbations.

Overall, the marker function M_k was effective in the eigenspace perturbation framework in constructing uncertainty bounds for both mean velocity and turbulence properties. Future work will focus on the development of different types of marker functions based on a variety of transitional flow scenarios. Eigenvector perturbations to the Reynolds stress tensor should also be conducted to complete the full range of the model form uncertainty in the Boussinesq turbulent viscosity models. Also a wider range of RANS based transition models will be tested using the eigenspace perturbation framework with marker involved.

ACKNOWLEDGMENTS

The support of the Natural Sciences and Engineering Research Council (NSERC) of Canada for the research program of Professor Xiaohua Wu and Professor David E. Rival is gratefully acknowledged.

DATA AVAILABILITY STATEMENT

The data that support the findings of this study are available from the corresponding author upon reasonable request.

REFERENCES

- ¹R. Pecnik and W. Sanz, "Application of the turbulent potential model to heat transfer predictions on a turbine guide vane," (2007).
- ²F. Menter, T. Esch, and S. Kubacki, "Transition modelling based on local variables," in *Engineering Turbulence Modelling and Experiments 5* (Elsevier, 2002) pp. 555–564.
- ³F. Menter, R. Langtry, S. Likki, Y. Suzen, P. Huang, and S. Voelker, "A correlation-based transition model using local variables: Part I—model formulation," in *Turbo Expo: Power for Land, Sea, and Air*, Vol. 41693 (2004) pp. 57–67.
- ⁴F. Menter, R. Langtry, and S. Voelker, "Transition modelling for general purpose cfd codes," *Flow, turbulence and combustion* **77**, 277–303 (2006).
- ⁵R. B. Langtry and F. R. Menter, "Correlation-based transition modeling for unstructured parallelized computational fluid dynamics codes," *AIAA journal* **47**, 2894–2906 (2009).
- ⁶F. R. Menter, P. E. Smirnov, T. Liu, and R. Avancha, "A one-equation local correlation-based transition model," *Flow, Turbulence and Combustion* **95**, 583–619 (2015).
- ⁷L. Wei, X. Ge, J. George, and P. Durbin, "Modeling of laminar-turbulent transition in boundary layers and rough turbine blades," *Journal of Turbomachinery* **139** (2017).
- ⁸N. Tousi, M. Coma, J. Bergada, J. Pons-Prats, F. Mellibovsky, and G. Bugea, "Active flow control optimisation on sd7003 airfoil at pre and post-stall angles of attack using synthetic jets," *Applied Mathematical Modelling* **98**, 435–464 (2021).
- ⁹M. Emory, J. Larsson, and G. Iaccarino, "Modeling of structural uncertainties in reynolds-averaged navier-stokes closures," *Physics of Fluids* **25**, 110822 (2013).
- ¹⁰M. Emory, V. Terrapon, R. Pecnik, and G. Iaccarino, "Characterizing the operability limits of the hyshot ii scramjet through rans simulations," in *17th AIAA international space planes and hypersonic systems and technologies conference* (2011) p. 2282.
- ¹¹C. Górlé, S. Zeoli, M. Emory, J. Larsson, and G. Iaccarino, "Epistemic uncertainty quantification for reynolds-averaged navier-stokes modeling of separated flows over streamlined surfaces," *Physics of Fluids* **31**, 035101 (2019).
- ¹²A. Mishra and G. Iaccarino, "Rans predictions for high-speed flows using enveloping models," arXiv preprint arXiv:1704.01699 (2017).
- ¹³G. Iaccarino, A. A. Mishra, and S. Ghili, "Eigenspace perturbations for uncertainty estimation of single-point turbulence closures," *Physical Review Fluids* **2**, 024605 (2017).
- ¹⁴L. F. Cremades Rey, D. F. Hinz, and M. Abkar, "Reynolds stress perturbation for epistemic uncertainty quantification of rans models implemented in openfoam," *Fluids* **4**, 113 (2019).
- ¹⁵N. Razaaly, G. Gori, G. Iaccarino, and P. M. Congedo, "Optimization of an orc supersonic nozzle under epistemic uncertainties due to turbulence models," in *GPPS 2019-Global Power and Propulsion Society* (2019).
- ¹⁶L. W. Cook, A. Mishra, J. Jarrett, K. Willcox, and G. Iaccarino, "Optimization under turbulence model uncertainty for aerospace design," *Physics of Fluids* **31**, 105111 (2019).
- ¹⁷A. A. Mishra, J. Mukhopadhyaya, J. Alonso, and G. Iaccarino, "Design exploration and optimization under uncertainty," *Physics of Fluids* **32**, 085106 (2020).
- ¹⁸M. Matha and C. Morsbach, "Extending turbulence model uncertainty quantification using machine learning," arXiv preprint arXiv:2202.01560 (2022).
- ¹⁹M. Matha, K. Kucharczyk, and C. Morsbach, "Assessment of data-driven reynolds stress tensor perturbations for uncertainty quantification of rans turbulence models," in *AIAA AVIATION 2022 Forum* (2022) p. 3767.
- ²⁰C. García-Sánchez, D. Philips, and C. Górlé, "Quantifying inflow uncertainties for cfd simulations of the flow in downtown oklahoma city," *Building and environment* **78**, 118–129 (2014).
- ²¹C. Górlé, C. Garcia-Sanchez, and G. Iaccarino, "Quantifying inflow and rans turbulence model form uncertainties for wind engineering flows," *Journal of Wind Engineering and Industrial Aerodynamics* **144**, 202–212 (2015).
- ²²H. Xiao, J.-L. Wu, J.-X. Wang, R. Sun, and C. Roy, "Quantifying and reducing model-form uncertainties in reynolds-averaged navier-stokes simulations: A data-driven, physics-informed bayesian approach," *Journal of Computational Physics* **324**, 115–136 (2016).
- ²³J.-L. Wu, J.-X. Wang, and H. Xiao, "A bayesian calibration–prediction method for reducing model-form uncertainties with application in rans simulations," *Flow, Turbulence and Combustion* **97**, 761–786 (2016).
- ²⁴E. J. Parish and K. Duraisamy, "A paradigm for data-driven predictive modeling using field inversion and machine learning," *Journal of Computational Physics* **305**, 758–774 (2016).
- ²⁵H. Xiao, J.-X. Wang, and R. G. Ghanem, "A random matrix approach for quantifying model-form uncertainties in turbulence modeling," *Computer Methods in Applied Mechanics and Engineering* **313**, 941–965 (2017).
- ²⁶J.-X. Wang, J.-L. Wu, and H. Xiao, "Physics-informed machine learning approach for reconstructing reynolds stress modeling discrepancies based on dns data," *Physical Review Fluids* **2**, 034603 (2017).
- ²⁷J.-X. Wang, J. Wu, J. Ling, G. Iaccarino, and H. Xiao, "A comprehensive physics-informed machine learning framework for predictive turbulence modeling," arXiv preprint arXiv:1701.07102 (2017).
- ²⁸J. F. Heyse, A. A. Mishra, and G. Iaccarino, "Estimating rans model uncertainty using machine learning," *Journal of the Global Power and Propulsion Society* **2021**, 1–14 (2021).
- ²⁹J. Mukhopadhyaya, B. T. Whitehead, J. F. Quindlen, J. J. Alonso, and A. W. Cary, "Multi-fidelity modeling of probabilistic aerodynamic databases for use in aerospace engineering," *International Journal for Uncertainty Quantification* **10** (2020).
- ³⁰N. Nigam, S. Mohseni, J. Valverde, S. Voronin, J. Mukhopadhyaya, and J. J. Alonso, "A toolset for creation of multi-fidelity probabilistic aerodynamic databases," in *AIAA Scitech 2021 Forum* (2021) p. 0466.
- ³¹A. Mishra and G. Iaccarino, "Theoretical analysis of tensor perturbations for uncertainty quantification of reynolds averaged and subgrid scale closures," *Physics of Fluids* **31**, 075101 (2019).
- ³²C. Górlé and G. Iaccarino, "A framework for epistemic uncertainty quantification of turbulent scalar flux models for reynolds-averaged navier-stokes simulations," *Physics of Fluids* **25**, 055105 (2013).
- ³³C. Górlé, J. Larsson, M. Emory, and G. Iaccarino, "The deviation from parallel shear flow as an indicator of linear eddy-viscosity model inaccuracy," *Physics of Fluids* **26**, 055105 (2014).
- ³⁴H. Zhang, *Turbulent and Non-Turbulent Interfaces in Low Mach Number Airfoil Flows*, Ph.D. thesis, Queen's University (Canada) (2021).
- ³⁵F. Menter, "Zonal two equation kw turbulence models for aerodynamic flows," in *23rd fluid dynamics, plasmadynamics, and lasers conference* (1993) p. 2906.
- ³⁶A. Hellsten, "Some improvements in menter's k-omega sst turbulence model," in *29th AIAA, Fluid Dynamics Conference* (1998) p. 2554.
- ³⁷F. Menter and T. Esch, "Elements of industrial heat transfer predictions," in *16th Brazilian Congress of Mechanical Engineering (COBEM)*, Vol. 109 (sn, 2001) pp. 117–127.
- ³⁸F. R. Menter, M. Kuntz, and R. Langtry, "Ten years of industrial experience with the sst turbulence model," *Turbulence, heat and mass transfer* **4**, 625–632 (2003).
- ³⁹S. B. Pope, "Turbulent flows," (2001).
- ⁴⁰M. Emory, R. Pecnik, and G. Iaccarino, "Modeling structural uncertainties in reynolds-averaged computations of shock/boundary layer interactions," in *49th AIAA Aerospace Sciences Meeting including the New Horizons Forum and Aerospace Exposition* (2011) p. 479.
- ⁴¹C. Górlé, M. Emory, J. Larsson, and G. Iaccarino, "Epistemic uncertainty quantification for rans modeling of the flow over a wavy wall," *Center for turbulence research, annual research briefs*, 81–91 (2012).
- ⁴²S. Banerjee, R. Krahl, F. Durst, and C. Zenger, "Presentation of anisotropy properties of turbulence, invariants versus eigenvalue approaches," *Journal of Turbulence*, N32 (2007).
- ⁴³A. A. Mishra, J. Mukhopadhyaya, G. Iaccarino, and J. Alonso, "Uncertainty estimation module for turbulence model predictions in su2," *AIAA Journal* **57**, 1066–1077 (2019).
- ⁴⁴A. E. Winkelman and J. B. Barlow, "Flowfield model for a rectangular planform wing beyond stall," *AIAA Journal* **18**, 1006–1008 (1980).
- ⁴⁵S. D. Hornshøj-Møller, P. D. Nielsen, P. Foroughi, and M. Abkar, "Quantifying structural uncertainties in reynolds-averaged navier-stokes simulations of wind turbine wakes," *Renewable Energy* **164**, 1550–1558 (2021).
- ⁴⁶P. Catalano and R. Tognaccini, "Rans analysis of the low-reynolds number flow around the sd7003 airfoil," *Aerospace Science and Technology* **15**,

- 615–626 (2011).
- ⁴⁷J. H. Ferziger, M. Perić, and R. L. Street, *Computational methods for fluid dynamics*, Vol. 3 (Springer, 2002).
- ⁴⁸J. P. Van Doormaal and G. D. Raithby, “Enhancements of the simple method for predicting incompressible fluid flows,” *Numerical heat transfer* **7**, 147–163 (1984).
- ⁴⁹D. J. Garmann, M. R. Visbal, and P. D. Orkwis, “Comparative study of implicit and subgrid-scale model large-eddy simulation techniques for low-reynolds number airfoil applications,” *International Journal for Numerical Methods in Fluids* **71**, 1546–1565 (2013).
- ⁵⁰M. Galbraith and M. Visbal, “Implicit large eddy simulation of low-reynolds-number transitional flow past the sd7003 airfoil,” in *40th fluid dynamics conference and exhibit* (2010) p. 4737.
- ⁵¹M. S. Boutilier and S. Yarusevych, “Parametric study of separation and transition characteristics over an airfoil at low reynolds numbers,” *Experiments in fluids* **52**, 1491–1506 (2012).
- ⁵²C. De Santis, P. Catalano, and R. Tognaccini, “Model for enhancing turbulent production in laminar separation bubbles,” *AIAA Journal* , 1–15 (2021).
- ⁵³L. F. Bernardos, F. Richez, and V. Gleize, “Rans modeling of laminar separation bubbles around airfoils at low reynolds conditions,” in *AIAA Aviation 2019 Forum* (2019) p. 2922.
- ⁵⁴J. Monteith and M. Unsworth, *Principles of environmental physics: plants, animals, and the atmosphere* (Academic Press, 2013).
- ⁵⁵U. Rist, K. Augustin, and S. Wagner, “Numerical simulation of laminar separation-bubble control,” in *New Results in Numerical and Experimental Fluid Mechanics III* (Springer, 2002) pp. 181–188.
- ⁵⁶M. Kiya and K. Sasaki, “Structure of large-scale vortices and unsteady reverse flow in the reattaching zone of a turbulent separation bubble,” *Journal of Fluid Mechanics* **154**, 463–491 (1985).
- ⁵⁷K. Zhang and D. E. Rival, “Direct lagrangian method to characterize entrainment dynamics using particle residence time: A case study on a laminar separation bubble,” *Experiments in Fluids* (2020).
- ⁵⁸M. Gaster, *The structure and behaviour of laminar separation bubbles* (Citeseer, 1967).
- ⁵⁹P. R. Spalart and M. K. Strelets, “Mechanisms of transition and heat transfer in a separation bubble,” *Journal of Fluid Mechanics* **403**, 329–349 (2000).
- ⁶⁰D. Lengani, D. Simoni, M. Ubaldi, and P. Zunino, “Pod analysis of the unsteady behavior of a laminar separation bubble,” *Experimental thermal and fluid science* **58**, 70–79 (2014).
- ⁶¹H. K. Versteeg and W. Malalasekera, *An introduction to computational fluid dynamics: the finite volume method* (Pearson education, 2007).